CCDs for X-ray Astronomy

Mark Bautz, MIT Center for Space Research

Overview:

- What is a CCD?
- The Spectral Redistribution Function
- X-ray Detection Efficiency
- Event Processing and Background Discrimination
- Pileup
- Radiation Damage
- The Future of X-ray CCDs

CCD Structure Determines X-ray Response

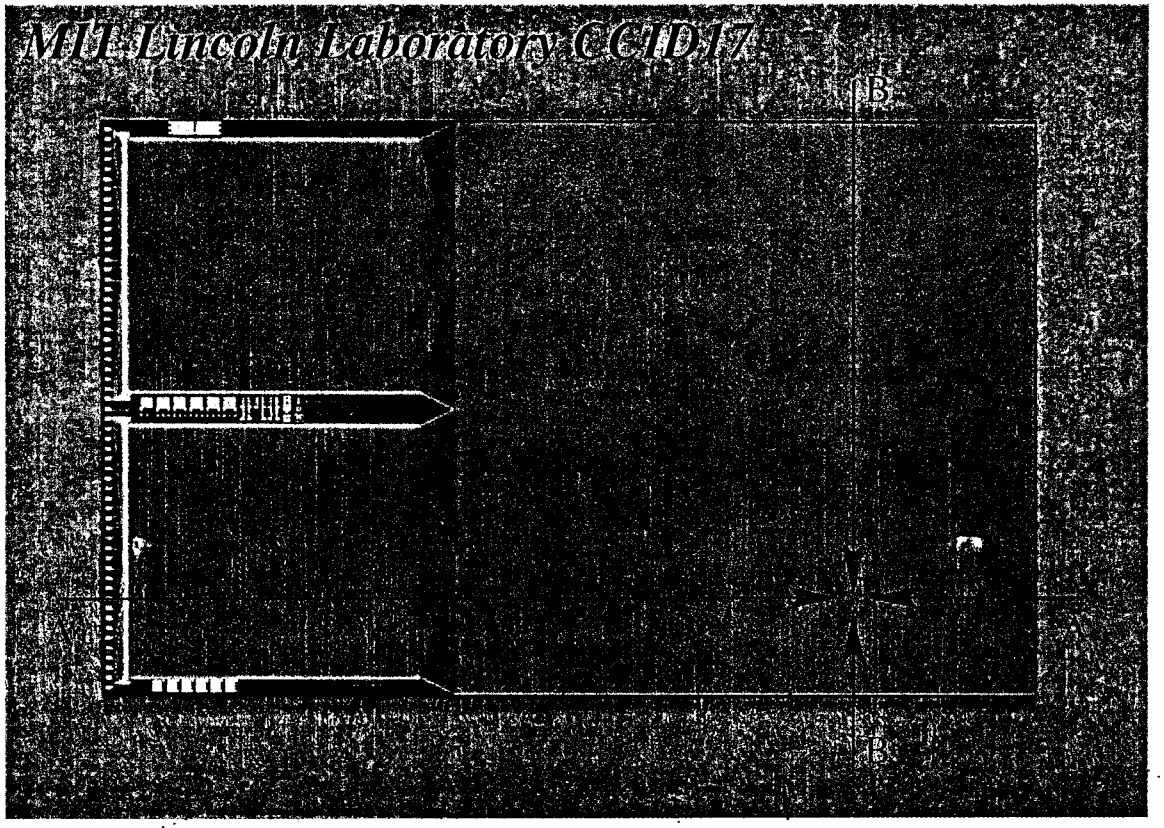

Section Through Gates Along Channel
(A-A)

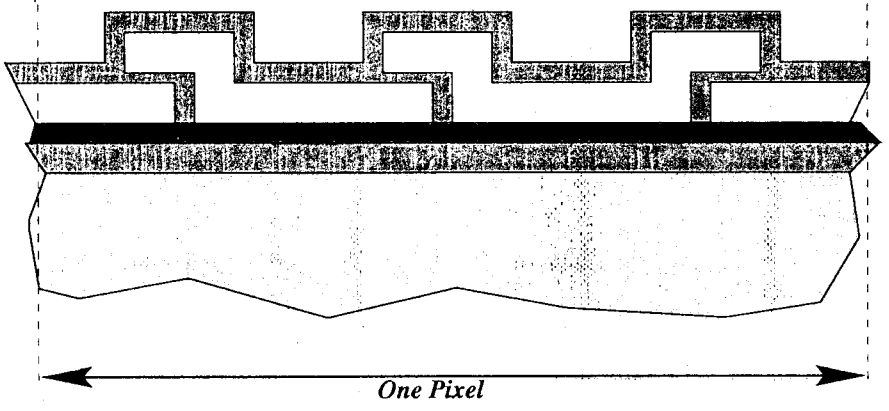

Section Through Channel Stops
(B-B)

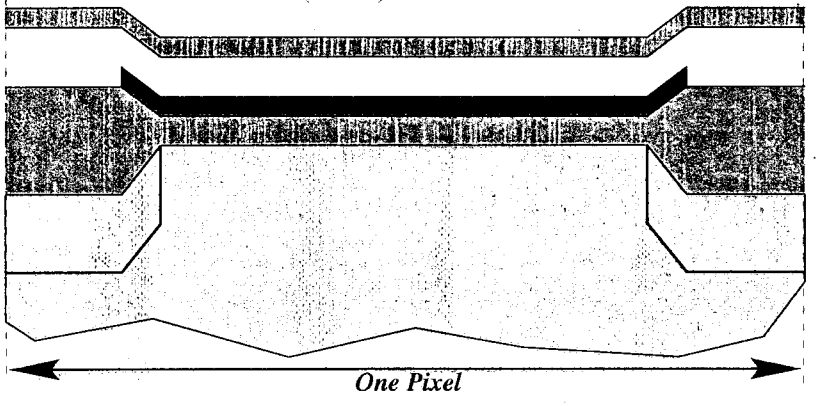

Soft-X-Ray CCD Imagers for AXAF

Barry E. Burke, *Senior Member, IEEE*, J. A. Gregory, M. W. Bautz, G. Y. Prigozhin, S. E. Kissel, Bernard B. Kosicki, *Senior Member, IEEE*, Andrew H. Loomis, and Douglas J. Young

Abstract—**We describe the key features and performance data of a 1024 × 1026-pixel frame-transfer imager for use as a soft-X-ray detector on the NASA X-ray observatory Advanced X-ray Astrophysics Facility (AXAF). The four-port device features a floating-diffusion output circuit with a responsivity of 20 $\mu V/e^-$ and noise of about 2 e^- at a 100-kHz data rate. Techniques for achieving the low sense-node capacitance of 5 fF are described. The CCD is fabricated on high-resistivity p-type silicon for deep depletion and includes narrow potential troughs for transfer inefficiencies of around 10^{-7}. To achieve good sensitivity at energies below 1 keV, we have developed a back-illumination process that features low recombination losses at the back surface and has produced quantum efficiencies of about 0.7 at 277 eV (carbon Kα).**

I. Introduction

CURRENTLY, CCD imagers are well-established as soft-X-ray spectroscopic detectors. This technology, with the combination of low noise (2 e^-), large area, and mechanical ruggedness, has eclipsed the tube-based technologies such as the gas-scintillation proportional counters. The best solid-state detectors, such as Si(Li) detectors, have higher noise and must operate at lower temperatures than CCD's. Two CCD focal planes based on four-chip 420 × 420-pixel imager mosaics have now been operating for four years in the US/Japanese Advanced Satellite for Cosmology and Astrophysics (ASCA) [1]. Here, we describe the further development of CCD's for use in the Advanced X-ray Astrophysics Facility (AXAF) satellite [2]–[4].

For the AXAF sensors, several aspects of the earlier ASCA devices were improved. Primary among these were lower read noise, larger area devices, and better response at lower (<1 keV) energies. The packaging technology for AXAF has been in itself a major development but will not be described here. Improved read noise has resulted from an output circuit design which, among other things, utilizes buried contacts for a more compact sense node with reduced capacitance. The devices described here have a die size approximately four times larger than those of ASCA, and this was made possible by a transition from 75- to 100-mm wafers and a move from a class-100 fabrication facility to a new facility with near class-1 conditions. For improved low-energy response, we used a back-illumination process to avoid the large X-ray absorption losses below 1000 eV in the gate and dielectric layers of front-illuminated devices.

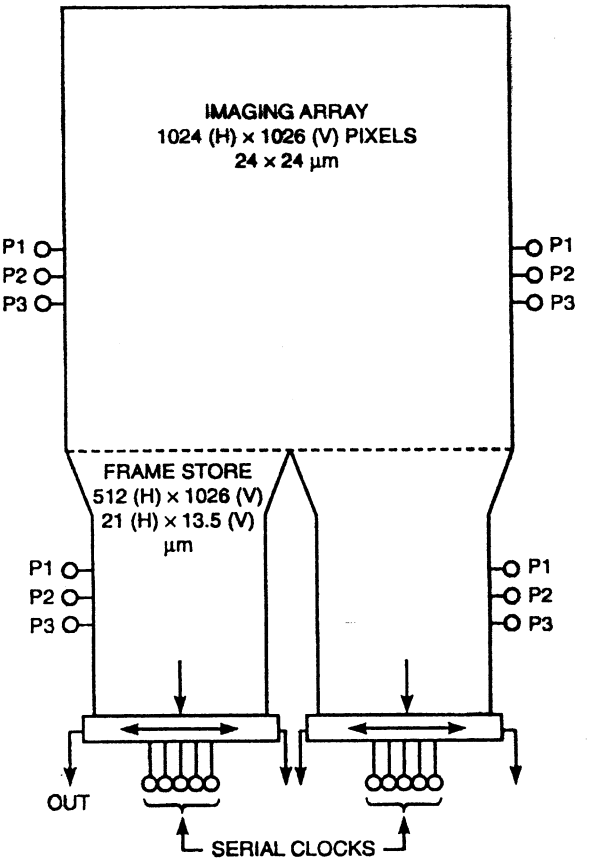

Fig. 1. Schematic of the 1024 × 1026-pixel CCD imager.

II. Device Design

A. Architecture and Process Overview

The architecture of the device, which is illustrated in Fig. 1, builds on the predecessor 420 × 420-pixel ASCA device and is likewise three-side abuttable. The sensor is made with a three-phase, triple-polysilicon process that has been described earlier [2], and the pixel sizes are 24 × 24 and 13.5 (V) × 21(H) μm in the imaging and nontapered frame-store regions, respectively. The frame stores are partitioned into left and right sections,

Manuscript received December 12, 1996; revised February 28, 1997. The review of this paper was arranged by Editor E. R. Fossum. This work was supported by the National Aeronautics and Space Administration and the Department of the Air Force. Opinions, interpretations, conclusions, and recommendations are those of the authors and are not necessarily endorsed by the United States Air Force.

B. E. Burke, J. A. Gregory, B. B. Kosicki, A. H. Loomis, and D. J. Young are with the Lincoln Laboratory, Massachusetts Institute of Technology, Lexington, MA 02173-9108 USA.

M. W. Bautz, G. Y. Prigozhin, and S. E. Kissel are with the Center for Space Research, Massachusetts Institute of Technology, Cambridge, MA 02139-4307 USA.

Publisher Item Identifier S 0018-9383(97)06912-8.

The number of electrons stored in a 4×8-μm^2 region is

$$N = (4 \times 10^{-4}) \times (8 \times 10^{-4}) \times (1.19 \times 10^{-7})/(1.6 \times 10^{-19}),$$

$$N = 2.4 \times 10^5 \, e^-.$$

It is important to note that the quantity of charge that can be stored is directly proportional to doping concentration and to the applied gate potential.

1.4.3 Buried-Channel Potential Well

Discussions above have described the operation of a surface-channel CCD, in which charge is stored and transferred along the surface of the semiconductor. As mentioned earlier, a major problem exists with surface-channel CCDs because signal charge is trapped at the Si–SiO_2 interface, severely limiting CTE performance. Early in the development of the CCD, different approaches were attempted to passivate and reduce the density of interface states. However, CTE requirements were too demanding even for the best of processes, especially for large-area-array scientific CCDs.

To avoid the surface-state problem, the buried-channel CCD was invented. In a buried-channel CCD, charge packets are confined to a channel (i.e., a potential well) that lies beneath the surface. In contrast to surface-channel operation, CTE performance for buried-channel CCDs is remarkably high. As demonstrated

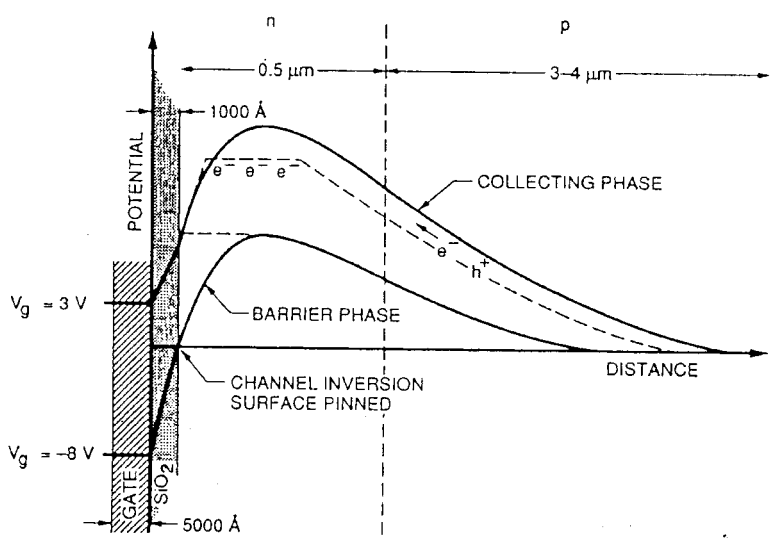

Figure 1.19 Buried-channel potential well.

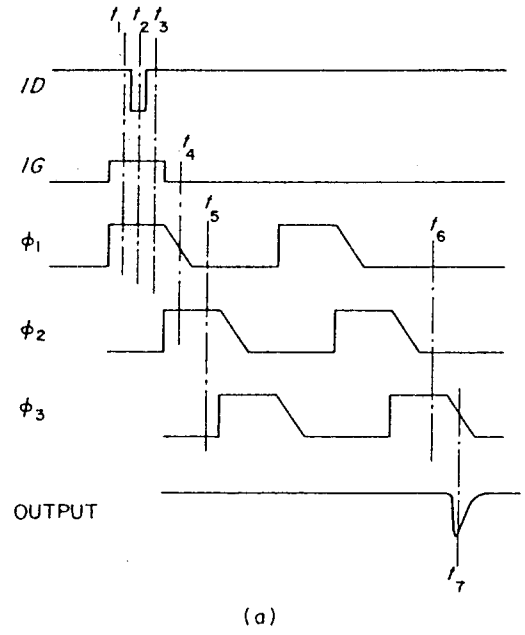

(a)

Figure 1.8 (a) Clock wave forms and output signal for the device shown in Figure 1.7. Output gate and output diode are d.c. biased.

under the ϕ_1 electrodes, therefore, will be higher than that under the ϕ_2 and ϕ_3 electrodes. If the distance between the electrodes (commonly called gap length) is sufficiently small, the transition from the high surface potential under a ϕ_1 electrode to the low surface potential under a ϕ_2 or ϕ_3 electrode will be smooth. This creates energy wells under the ϕ_1 electrodes as shown in Figure 1.8b. If we let the device stay in this condition for a long time, thermally generated electrons will be collected in the energy wells, forming charge packets stored in confined regions under ϕ_1 electrodes. In normal operation of a CCD, however, the clock frequency (frequency of the ϕ_1, ϕ_2 and ϕ_3 pulses) is sufficiently high for the number of thermally generated electrons to be negligible compared with the signal charge. The signal charge is injected into the device at $t = t_2$. At this time, the voltage of the input diode is lowered to a value between the surface potentials under the input gate and the ϕ_2 electrode. Electrons, then, find regions of lower potential and flow into the energy well under the ϕ_1 electrode through the input gate. At the end of this injection, the surface potentials under the input gate and the first ϕ_1 electrode will be the same as the input diode voltage. Electrons are now stored under the input gate and the first ϕ_1 electrode. At $t = t_3$, the voltage of the input diode is

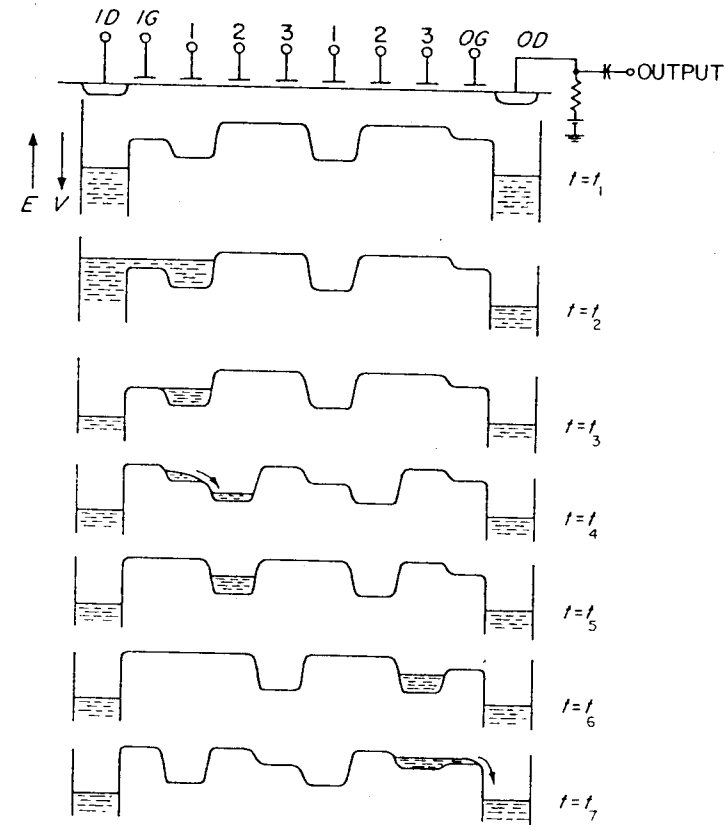

(b)

Figure 1.8 (b) Sketch of potential and charge distribution of the device shown in Figure 1.7 with the clocks shown in Figure 1.8a.

returned to a high value and the electrons under the input gate as well as the excess electrons under the first ϕ_1 electrode will be taken out of the device through the input diode lead. This creates a well-defined charge packet under the first ϕ_1 electrode. The size of the charge packet is proportional to the difference between the surface potential under the input gate and that of the first ϕ_1 electrode. It should be made clear at this point that the surface potential under the first ϕ_1 electrode at the end of the injection is the same as that under the input gate due to the lowering of the surface potential in the presence of the mobile electrons (see Figure 1.5). The surface potential under the ϕ_1 electrode to be used in determining the size of the charge packet is the surface potential when there are no mobile electrons. At $t = t_4$, the voltage applied to the ϕ_1 electrodes is returning to the low value while the ϕ_2 electrodes have high voltage applied to them. The electrons stored under the first ϕ_1 electrode are then moved to the first ϕ_2 electrode because

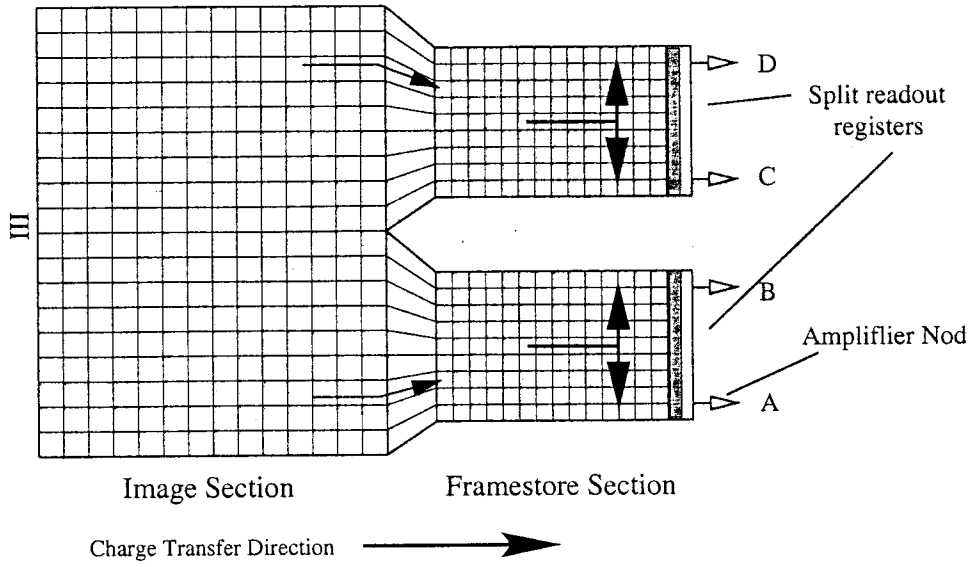
III
D
Split readout registers
C
B
Ampliflier Nod
A
Image Section
Framestore Section
Charge Transfer Direction

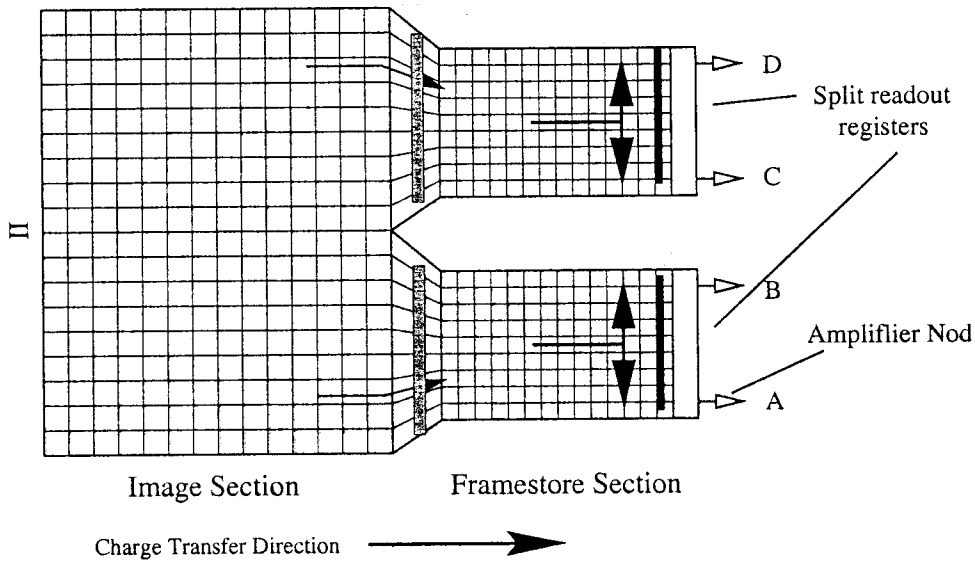
II
D
Split readout registers
C
B
Ampliflier Nod
A
Image Section
Framestore Section
Charge Transfer Direction

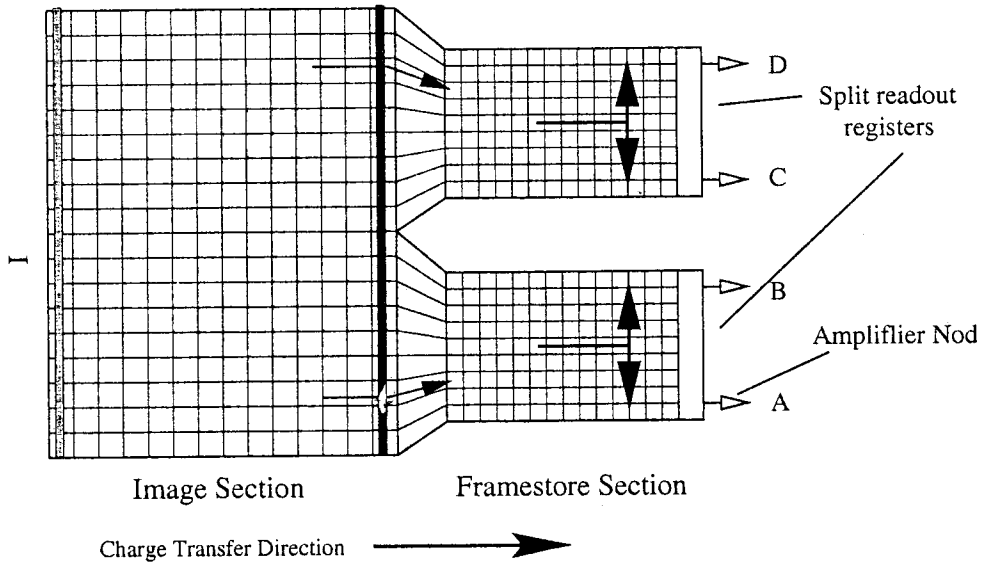
I
D
Split readout registers
C
B
Ampliflier Nod
A
Image Section
Framestore Section
Charge Transfer Direction

The Basic Idea

- Photoelectric interaction of a single X-ray photon with a Si atom in the CCD produces a measurable number of "free" electrons:

$$N_e = E_X/(3.65\,\mathrm{eV}) \quad (27 < N_e < 2700 \text{ for } 0.1 < 10\,\mathrm{keV})$$

$$\sigma_e^2 = 0.12 \times N_e \quad (\textit{not} \text{ a Poisson process})$$

- Spectral resolution depends on CCD readout noise and physics of secondary ionization:

$$\mathrm{FWHM(eV)} = 2.36 \times 3.65 \times \sqrt{\sigma_e^2 + \sigma_{read}^2}$$

- If the CCD is read sufficiently often that there is $<<$ 1 interaction per pixel per readout then it provides spectrally-resolved X-ray imaging.

- CCD characteristics that maximize spectral resolution include:

  ⋆ Good charge collection and transfer efficiencies at very low signal levels

  ⋆ Low readout and dark-current noise (low operating temperature)

  ⋆ High readout rate (requires tradeoff *vs.* noise)

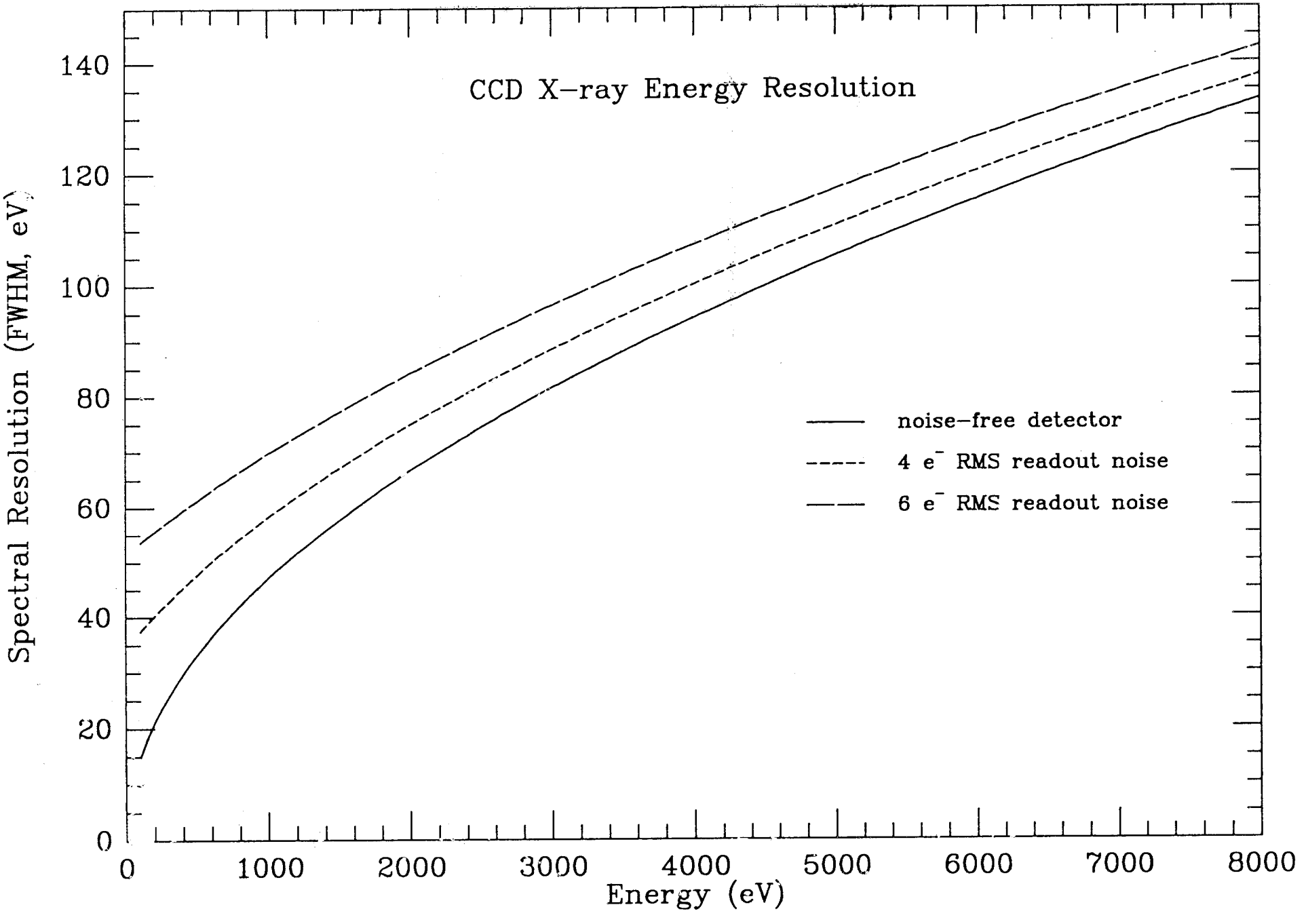
CCD X-ray Energy Resolution
Spectral Resolution (FWHM, eV)
Energy (eV)
0
20
40
60
80
100
120
140
0
1000
2000
3000
4000
5000
6000
7000
8000
noise-free detector
4 e⁻ RMS readout noise
6 e⁻ RMS readout noise

The Response Function Defined

Model Spectrum S(E)

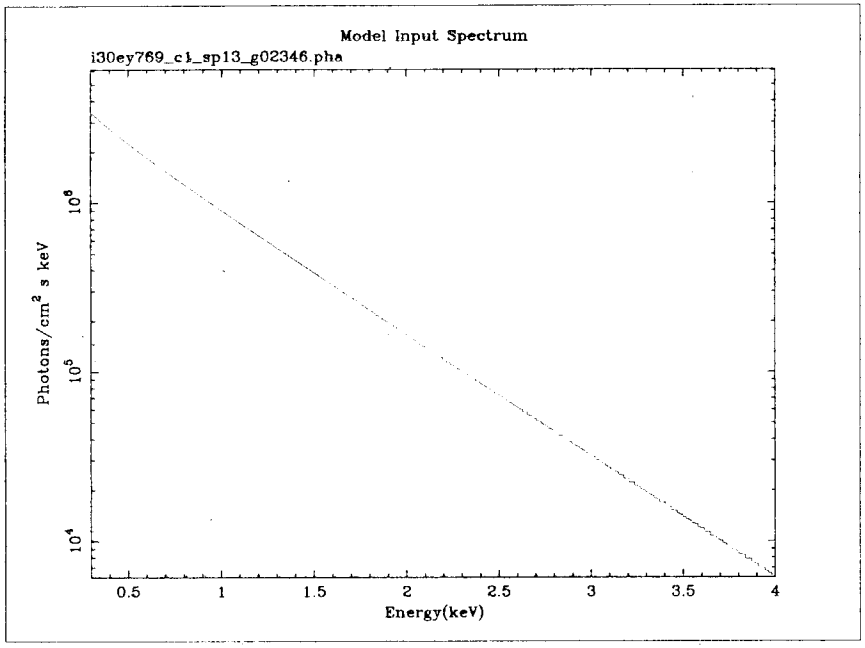

Response Function R(C,E)

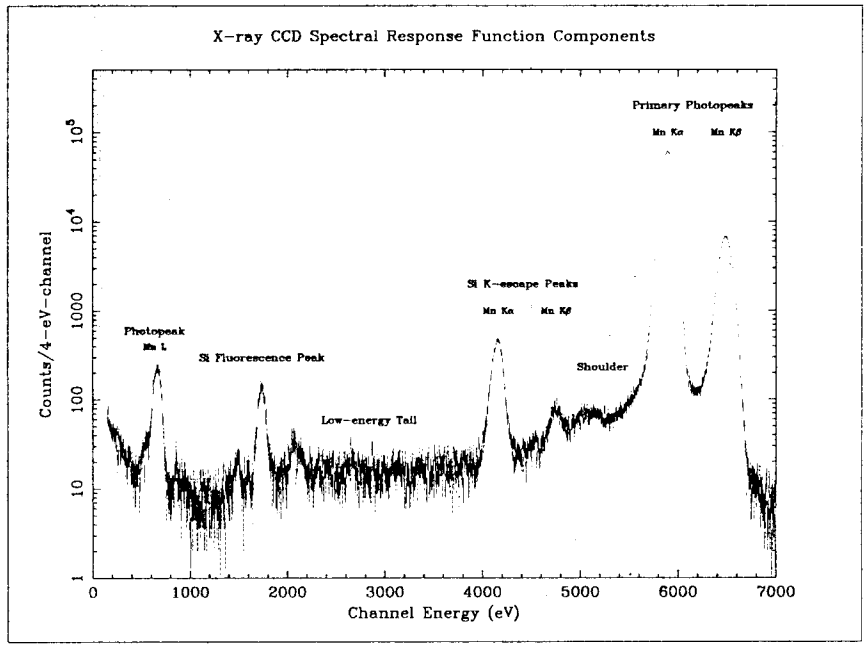

$$N(C) = \int S(E)\, R(C,E) dE$$

Data N(C) and Folded Model

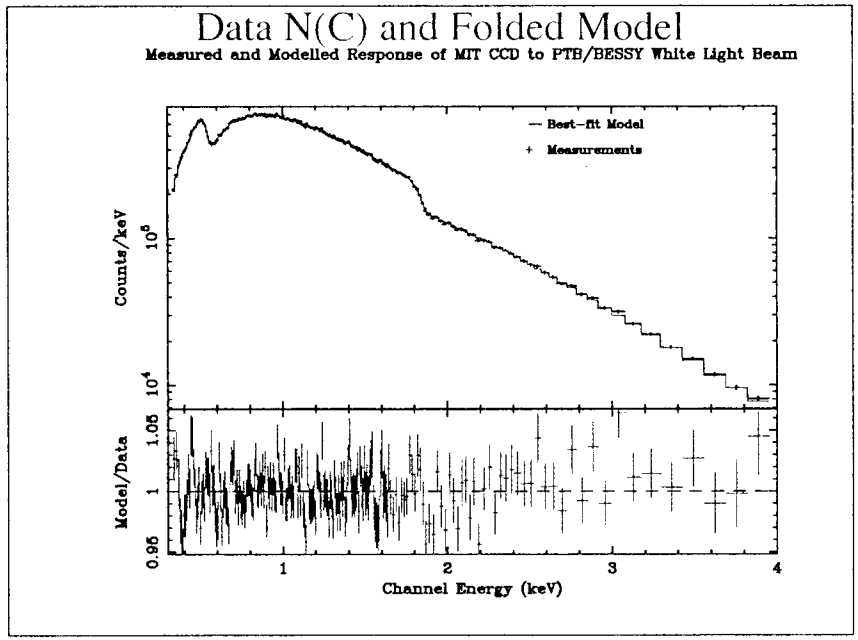

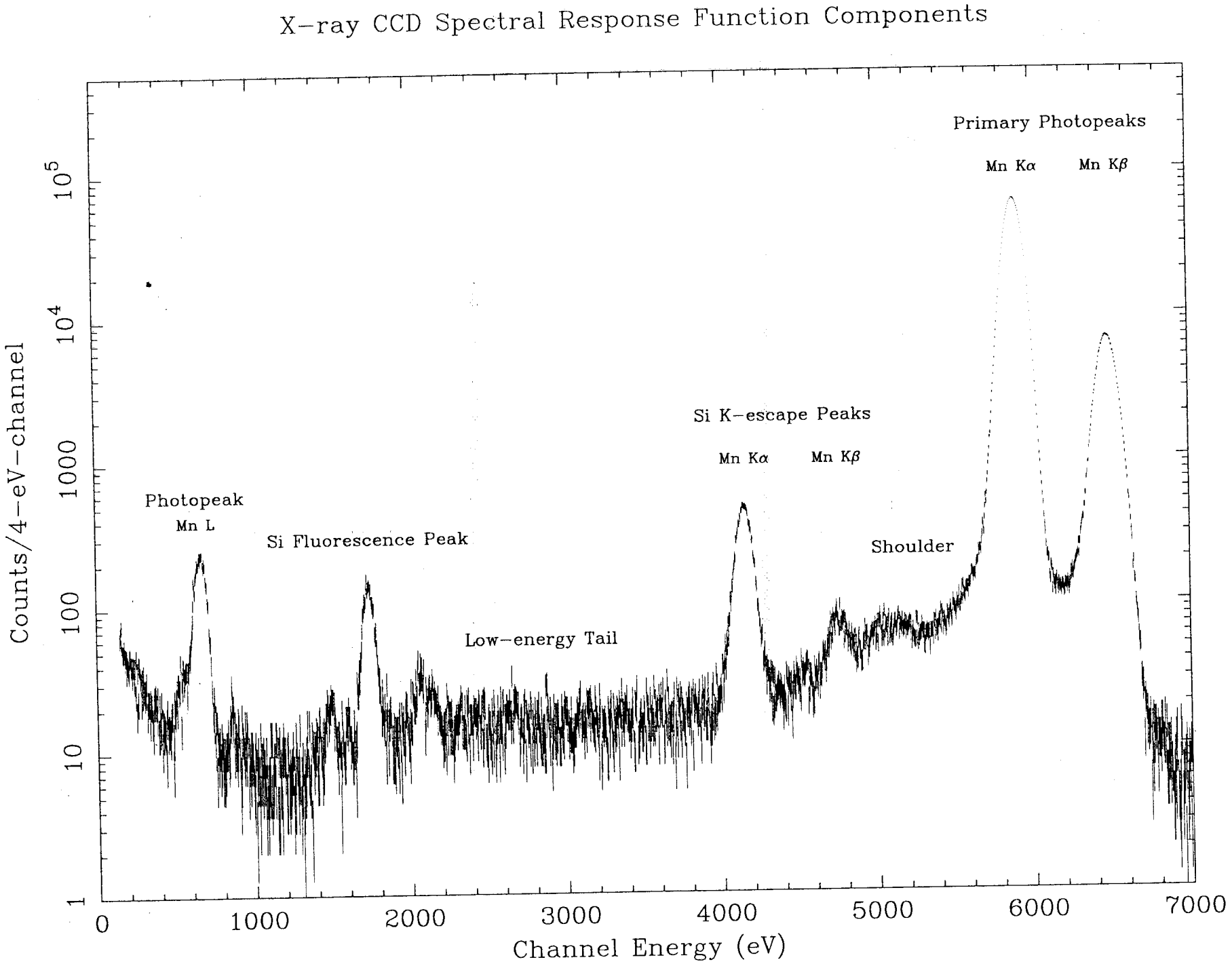
X-ray CCD Spectral Response Function Components
Primary Photopeaks
Mn Kα
Mn Kβ
Si K-escape Peaks
Mn Kα
Mn Kβ
Photopeak
Mn L
Si Fluorescence Peak
Low-energy Tail
Shoulder
Counts/4-eV-channel
1
10
100
1000
10^4
10^5
0
1000
2000
3000
4000
5000
6000
7000
Channel Energy (eV)

Front-Illuminated X-ray CCD Structure

(not to scale)

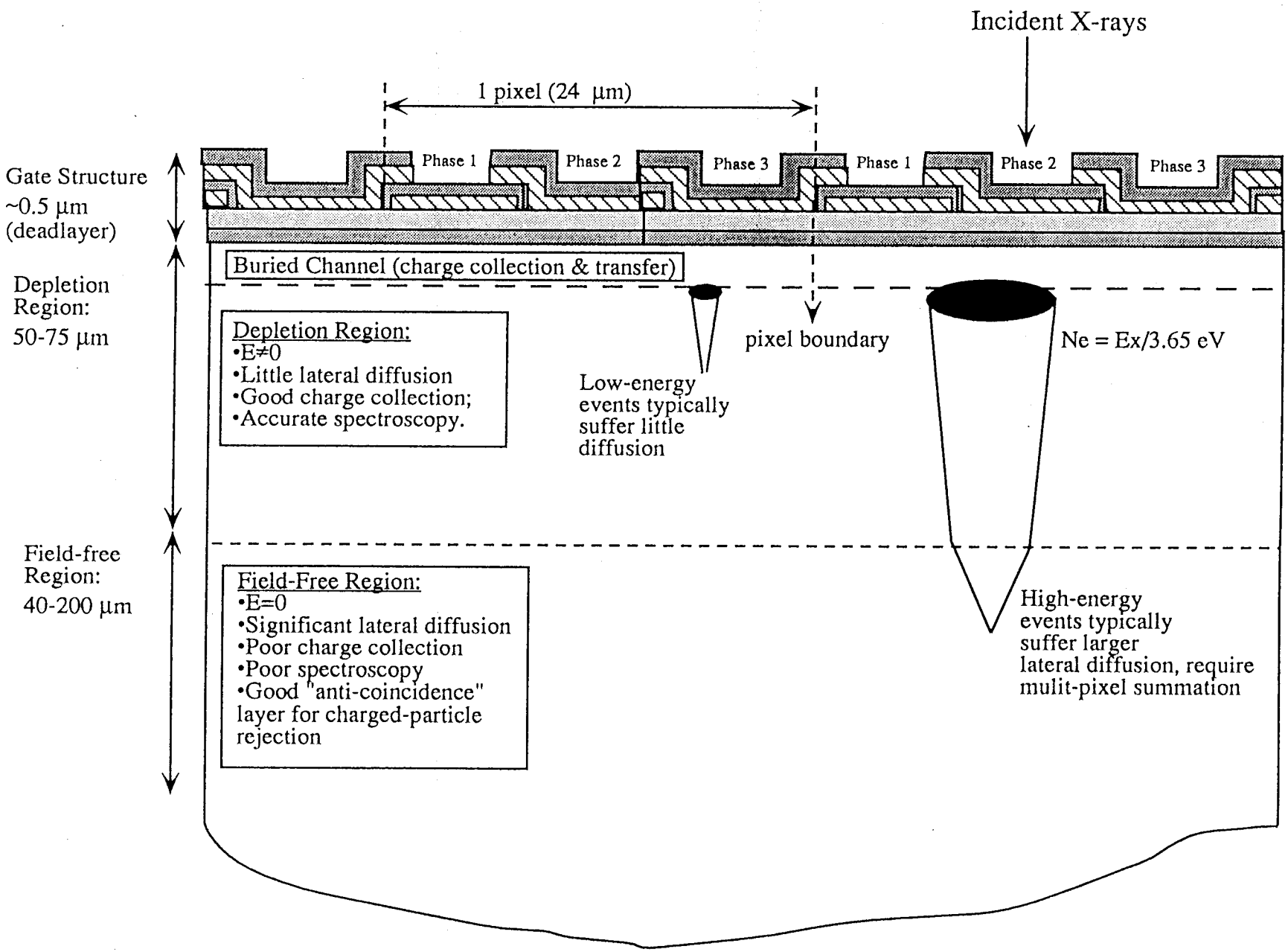

Schematic of Tail Model

Prigozhin et al., 1999 Nuclear Instruments and Methods (in press)

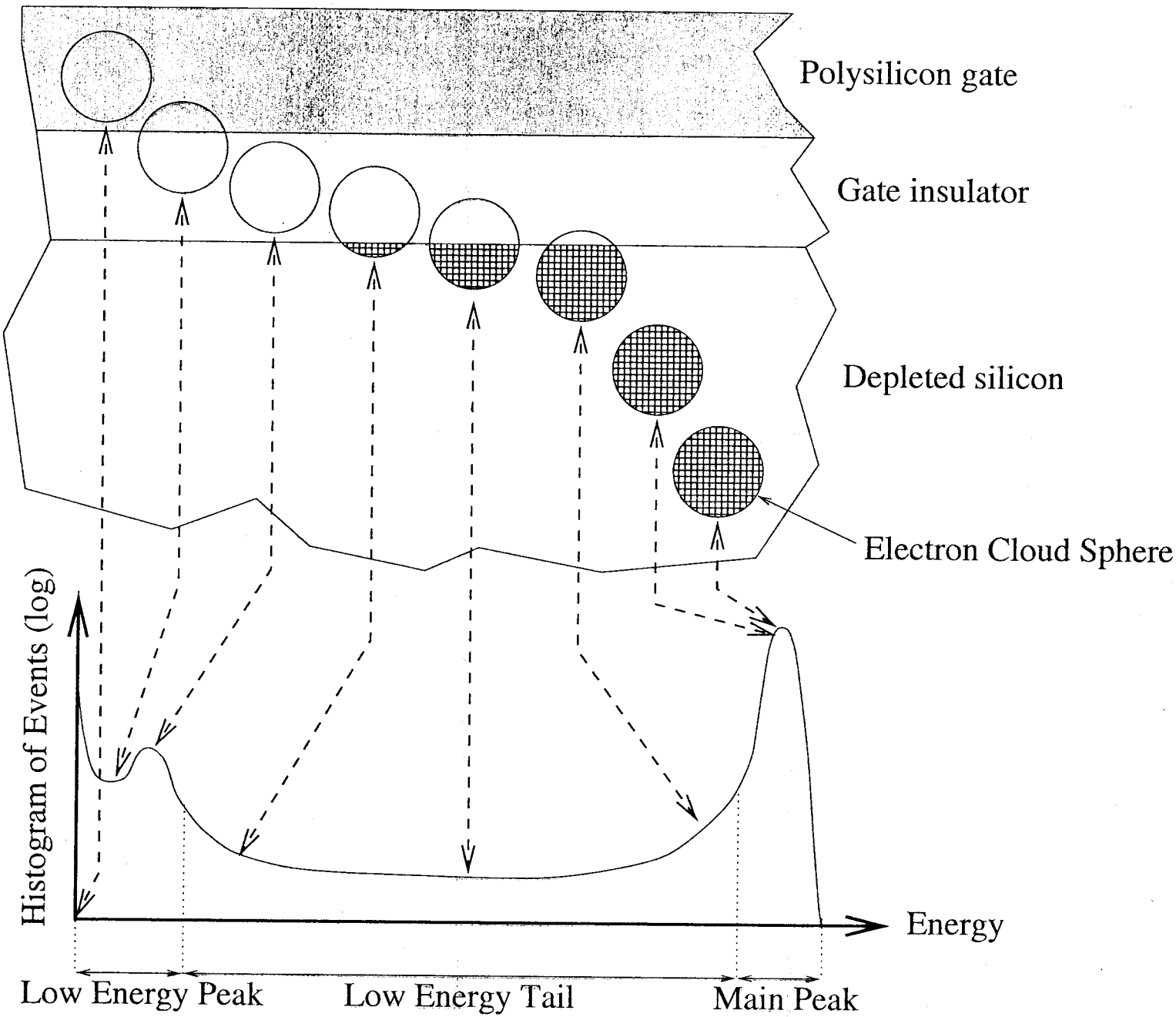

Chandra X-ray CCD Sensitivity Bands

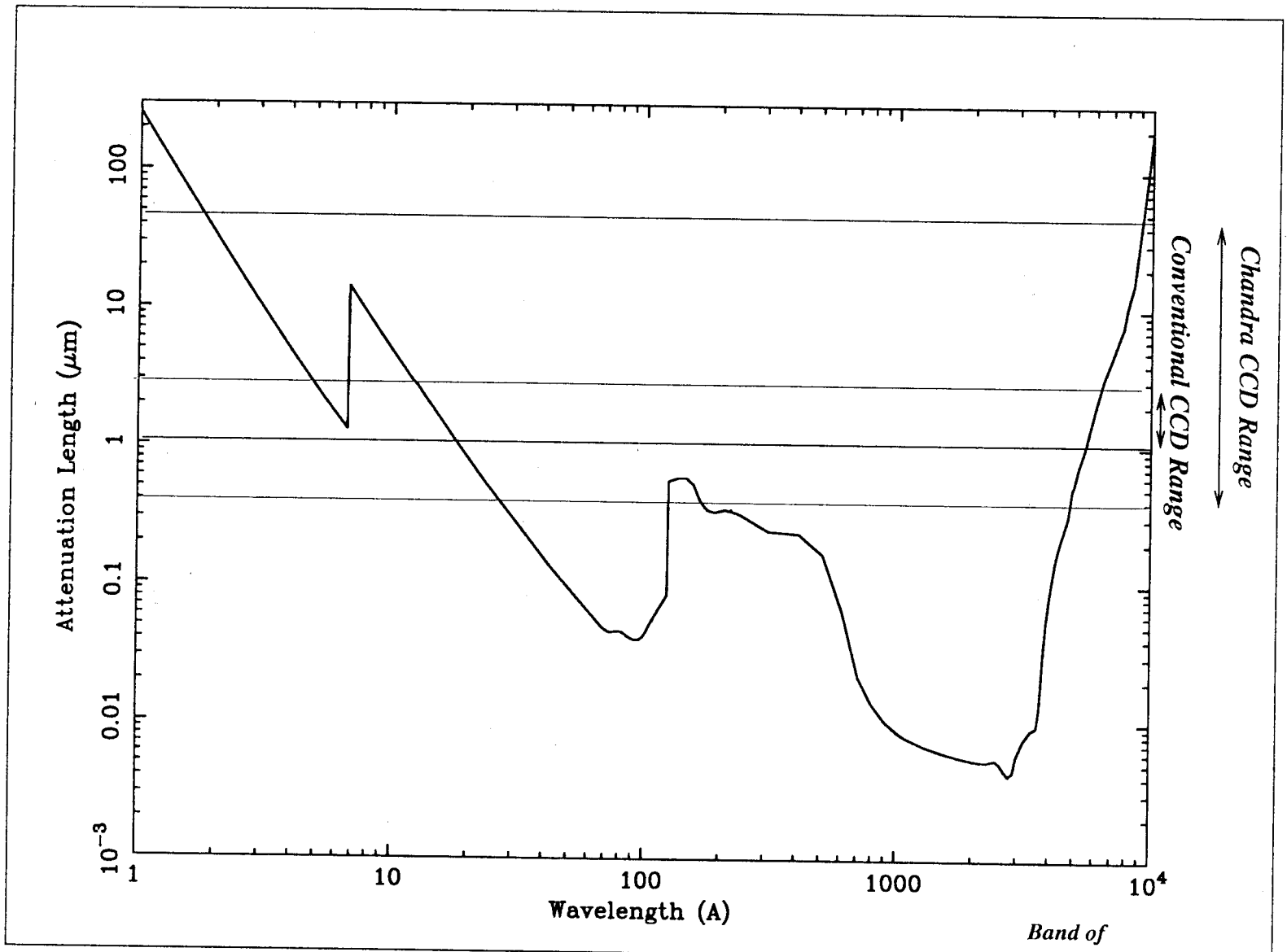

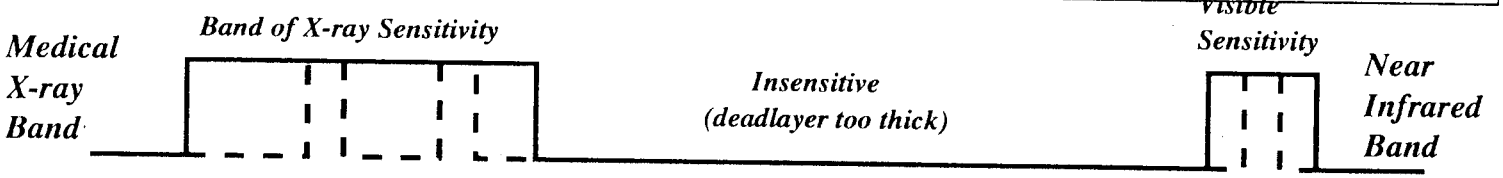

M. Bautz
MIT 1/99

ACIS Front– and Back–illuminated CCD Quantum Efficiencies

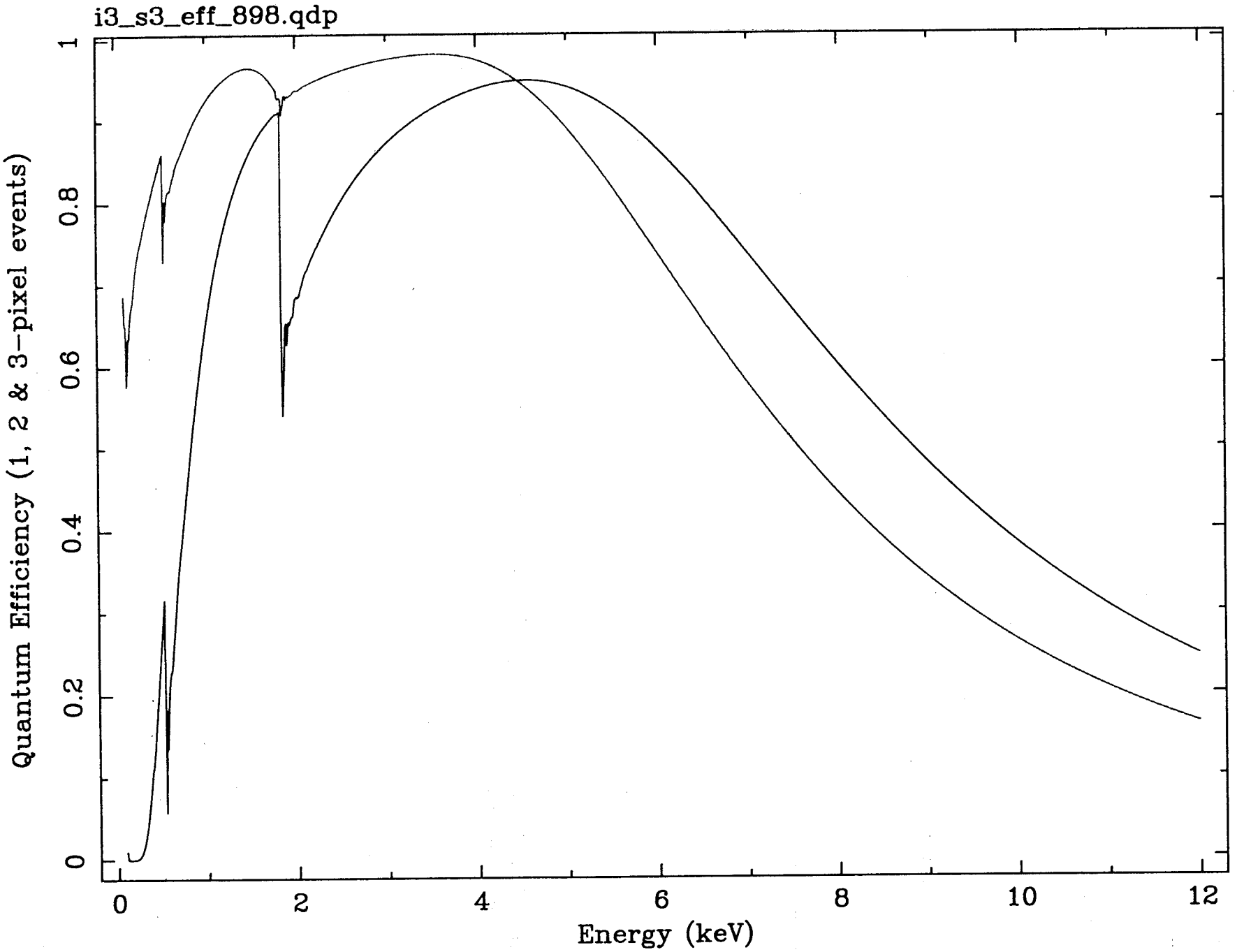

27–Nov–1998 16:22

Absorption Edge Structure in CCD Deadlayers

Prigozhin et al., 1998 Optical Engineering 37, 2848

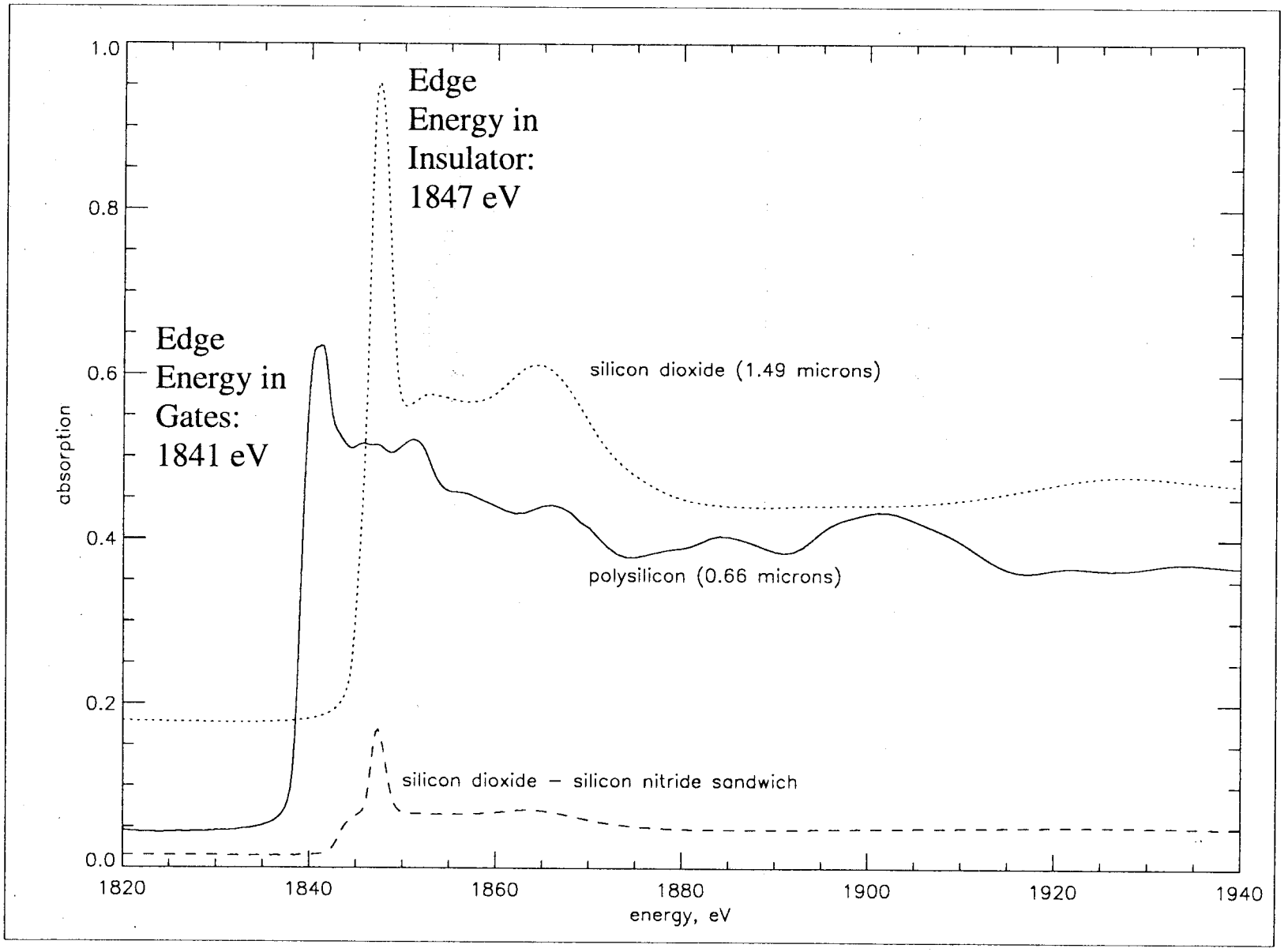

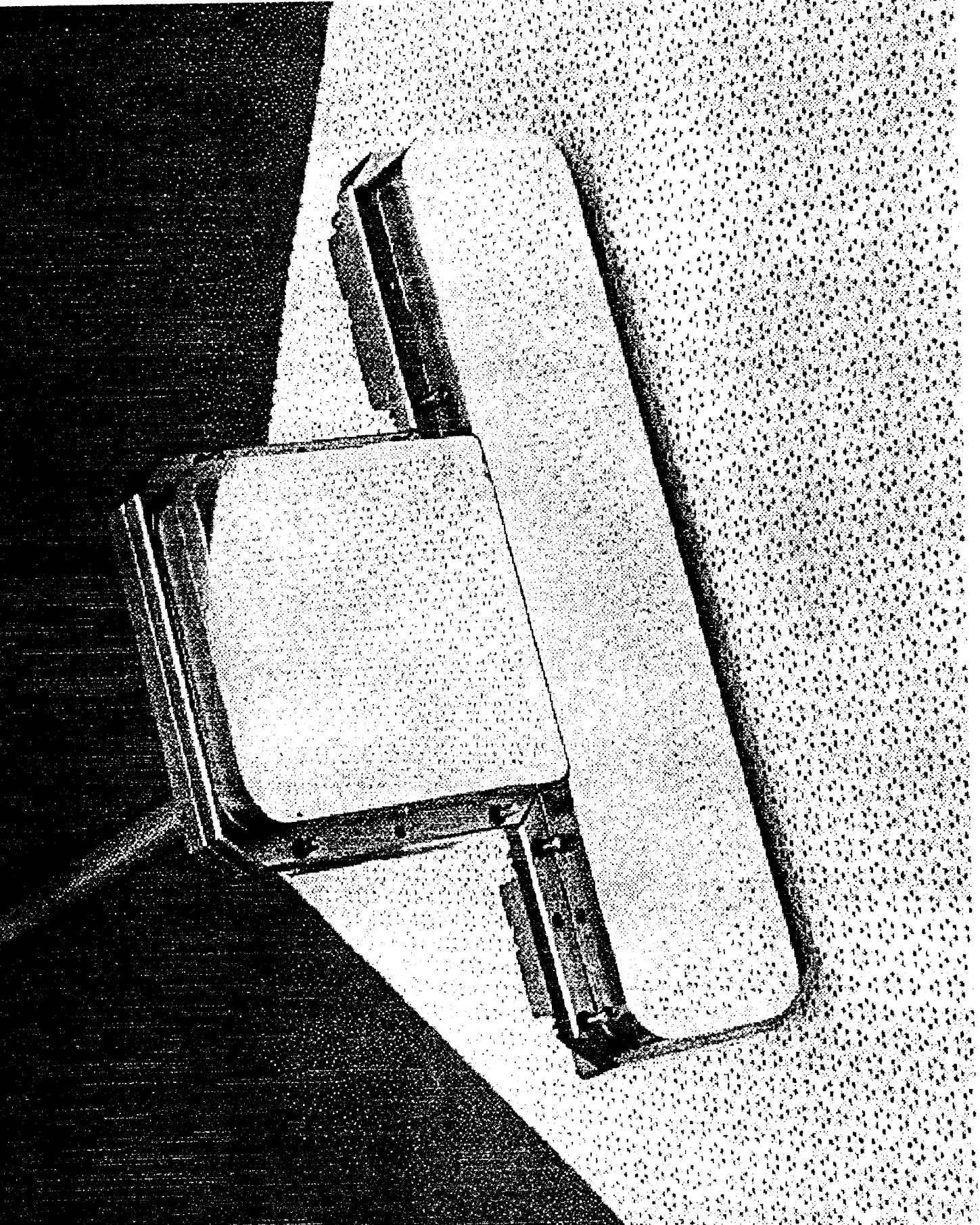

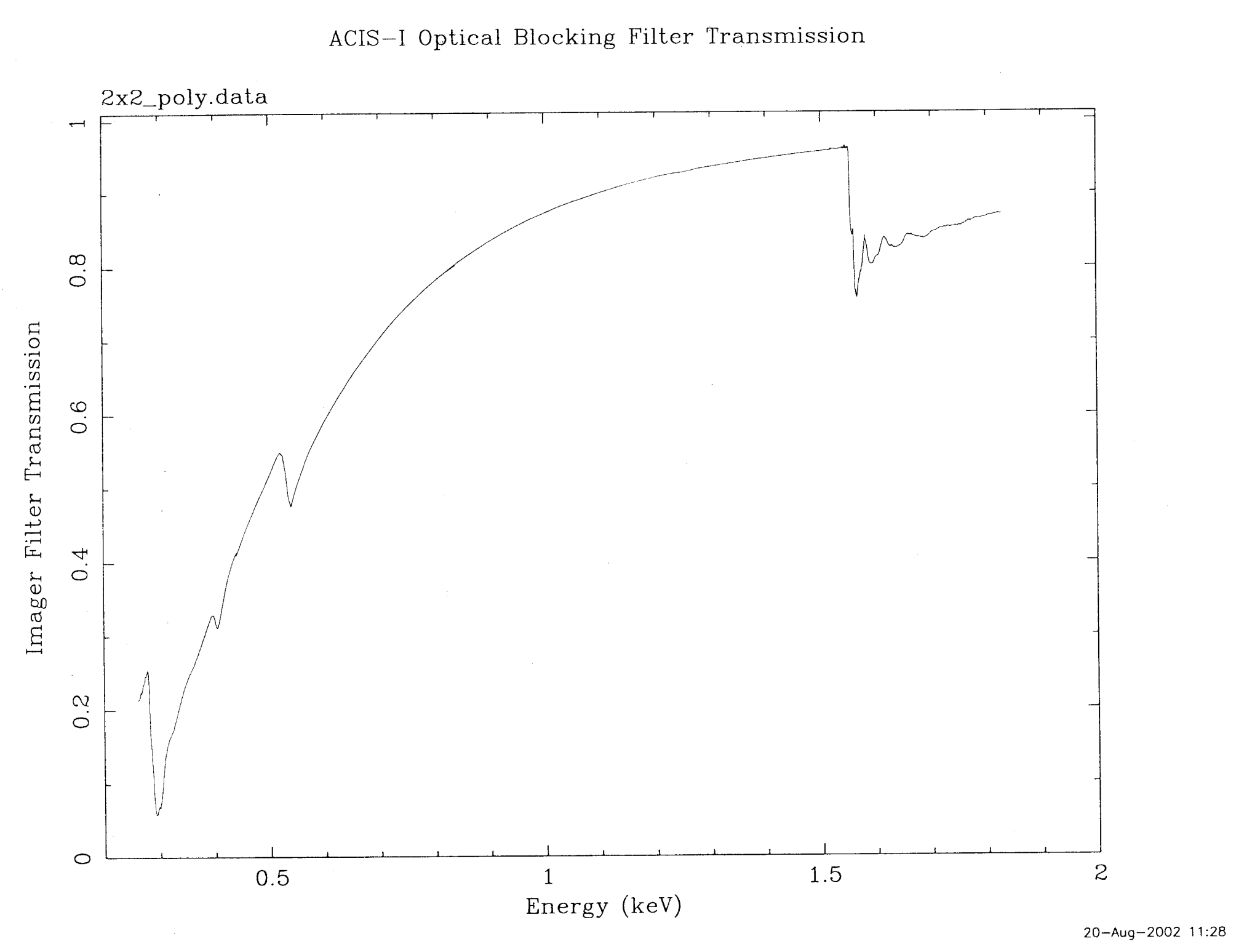
ACIS-I Optical Blocking Filter Transmission
2x2_poly.data
Imager Filter Transmission
0
0.2
0.4
0.6
0.8
1
0.5
1
1.5
2
Energy (keV)
20-Aug-2002 11:28

Galactic Column vs CCD Quantum Efficiency

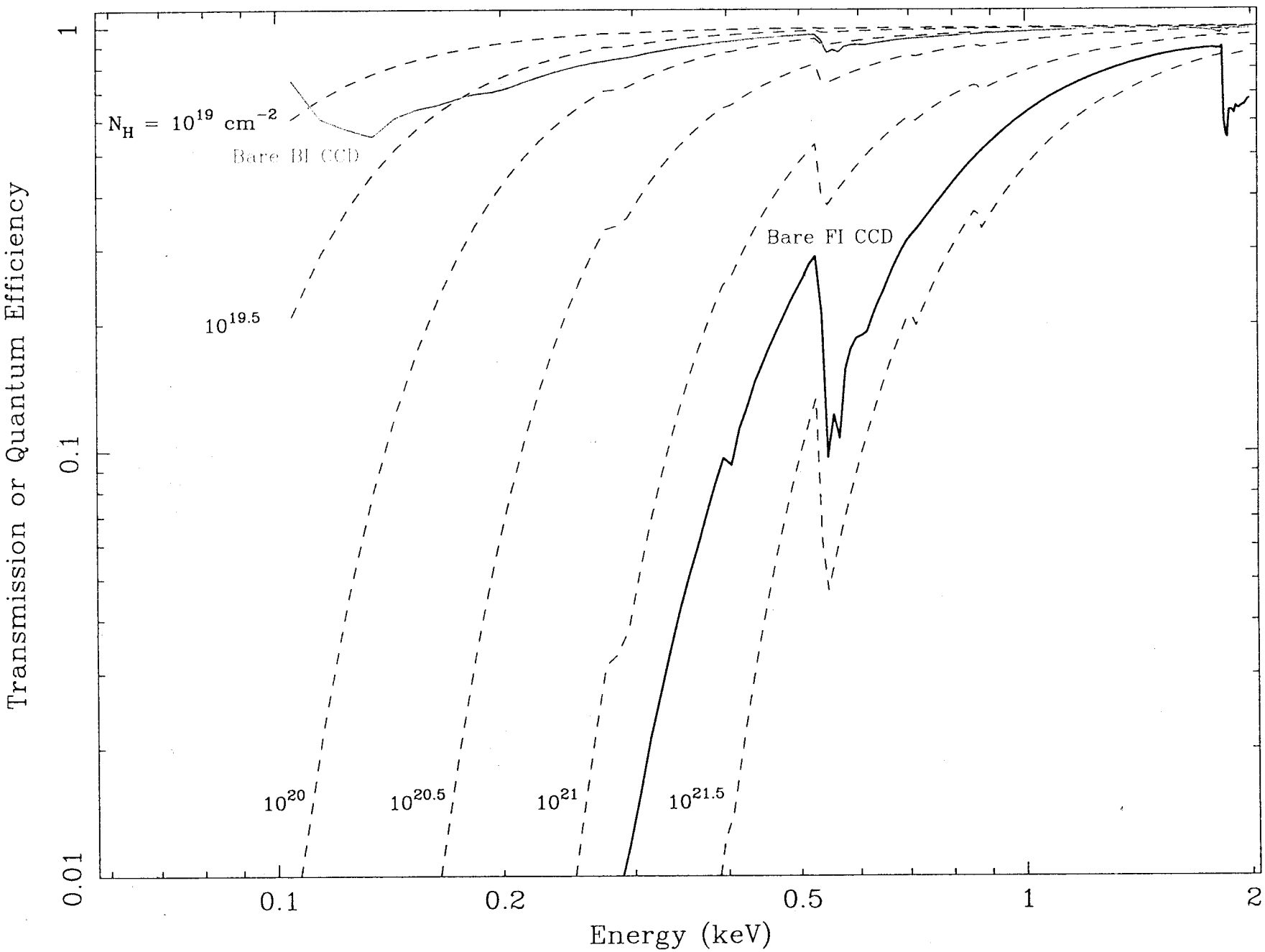

8-Aug-2002 11:55

Characteristics of Some "Current Generation" X-ray CCDs

Characteristic	Chandra-ACIS		XMM-Newton-EPIC	
	FI	BI	MOS	PN
Electrode Technology	3-poly MOS	3-poly MOS	3-poly MOS (open electrode)	Junction
Illumination	Front	Back	Front	Back
Pixel Size (μm)	24	24	40	150
Format	1k x 1k	1k x 1k	600 x 600	200 x 64
Detectors in Focal Plane	8	2	2 x 7	12
Focal Plane Sensitive Area (cm^2)	48 + 12		2 x 40	35
System Noise (e^-, RMS)	2	3	5	5
Single Channel Readout Rate (kpix s^{-1})	100	100	128	43
Readout Channels per Detector	4	4	1	64 analog + 1 A/D
Full Focal Plane Frame Time (s)	3.2	3.2	2.8	0.074
Charge Transfer Inefficiency	$< 3 \times 10^{-6}$	$< 1 - 3 \times 10^{-5}$	$< 3 \times 10^{-6}$	$\sim 10^{-4}$
Depletion Depth (μm)	75	40	40	300
Energy Resolution (eV, FWHM):				
at 0.525 keV	45	100	>80	70
at 5.9 keV	135	150	135	135
CCD Manufacturer	MIT/Lincoln	MIT/Lincoln	MAT (EEV)	MPE/HLL

Comparison of X-ray and Optical CCD Applications

Similarities

- Low noise is desirable (2-4 electrons RMS routine)
- Pixel size and area requirements are comparable
- Gate structure limits useful spectral range, so backside illumination is desirable

Differences

- X-ray devices must readout faster (~few s/frame) to count photons; requires framestore
- X-ray devices must have larger depletion depths (30-50 μm) for good QE and particle rejection; this requires higher resistivity (purer) silicon (by factor of $\sim 10^3$)
- X-ray devices must have extremely high charge transfer efficiency (CTI = (1-CTE) < 10^{-5}) at very low signal
- X-ray signal is very high contrast, so cross-talk rejection requirements may be more stringent
- X-ray devices have significant out-of-band sensitivity (e.g., UV, optical) that must be controlled
- Optical applications are more sensitive to pixel-to-pixel quantum efficiency variations (relatively high sky background), and optical response may be more sensitive to gate structure thickness variations
- Optical devices require relatively large full well capacity (by factor of 10-100) and larger dynamic range (16 bits vs 12 bits)

First Readout of ACIS CCDs

S2 = w182c4r

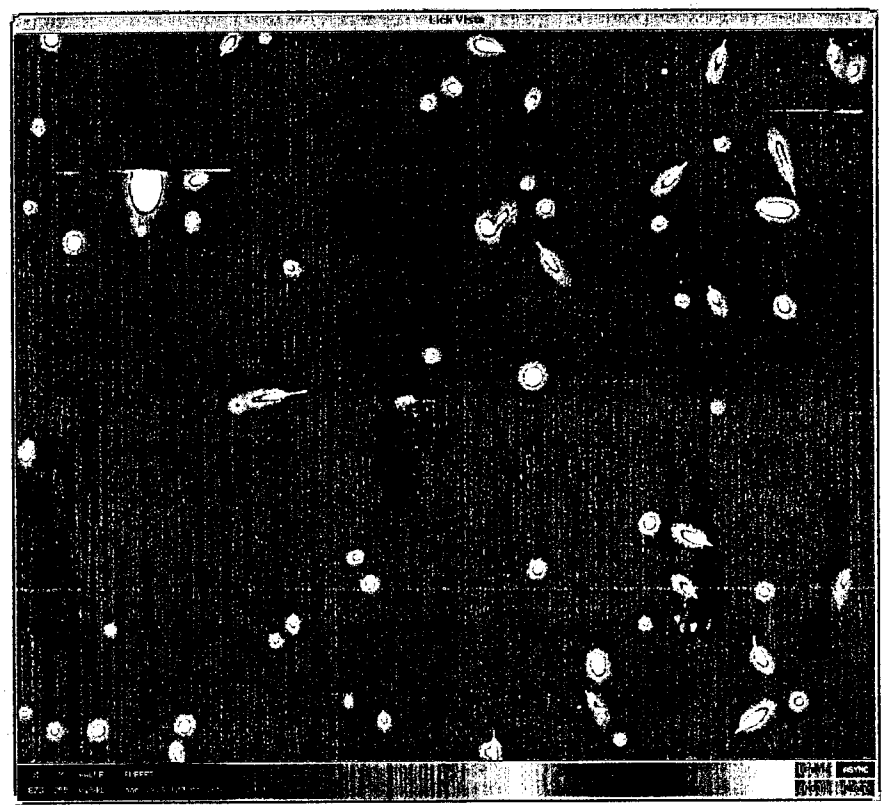

S3 = w134c4r

We first read charge from the ACIS CCD detectors on-orbit on July 27, 1999 at about 8:25pm local (EDT) time (209:01515Z). At this point the ACIS door was still closed and Chandra was not yet in its final orbit. The focal plane temperature was -90C. An an altitude of about 60,000km, we were greeted by a host of cosmic-ray and other particle tracks. The undepleted bulk of the front-illuminated device at focal plane position S2 (ccid17-182-4r) causes large and interesting particle tracks, especially when the interaction occurs in the framestore (the output register is at the top in these pictures.) The response of the thinner (40-micron-thick) back-illuminated chip at S3 (ccid17-134-4r) is much less alarming, but in the end the background rejection efficiency of the FI devices is better by a factor of 3. Some X-ray events from the ACIS Internal Calibration Source are visible at the top of the S3 image. For all 10 devices on the focal plane, the readout noise, as measured from the overclocked pixels, was found to be 2-3 electrons, RMS, just as it was on the ground. Exposure time for these images is about 3.3 seconds.

Data Processing Algorithms

- CCD output data rate (~10 Mbits/sec/ccd) far exceeds spacecraft telemetry resources
- Criteria for event: A pixel is the center of an event if:
  i) it exceeds the (commandable) event threshold, and
  ii) it is a local maximum (in 3x3 neighborhood)
- To send complete event information requires telemetry of at least 9 amplitudes (plus position information) = ~ 128 bits/event
- Good spectral resolution and effective background rejection require selection on the basis of event shape.
- Event shape is characterized by the number and location of neighbor pixels which exceed a "split" threshold
- Ideally, shape discrimination is done only on the ground; can be done onboard spacecraft to increase event throughput, at the expense of information content

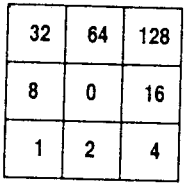

Figure 6.2: Schematic for determining the grade of an event. The grade is determined by summing the numbers for those pixels that are above their thresholds. For example, an event that caused all pixels to exceed their threshold is grade 255. A single pixel event is grade 0.

Table 6.2: ACIS and *ASCA* Grades

ACIS Grades	*ASCA* Grade	Description
0	0	Single pixel events
64 65 68 69	2	Vertical Split Up
2 34 130 162	2	Vertical Split Down
16 17 48 49	4/3	Horizontal Split Right
8 12 136 140	3/4	Horizontal Split Left
72 76 104 108	6	"L" & Quad, upper left
10 11 138 139	6	"L" & Quad, down left
18 22 50 54	6	"L" & Quad, down right
80 81 208 209	6	"L" & Quad, up right
1 4 5 32 128	1	Diagonal Split
33 36 37 129	1	
132 133 160 161	1	
164 165	1	
3 6 9 20 40	5	"L"-shaped split with corners
96 144 192 13 21	5	
35 38 44 52 53	5	
97 100 101 131	5	
134 137 141 145	5	
163 166 168 172	5	
176 177 193 196	5	
197	5	
24	7	3-pixel horizontal split
66	7	3-pixel vertical split
255	7	All pixels
All other grades	7	

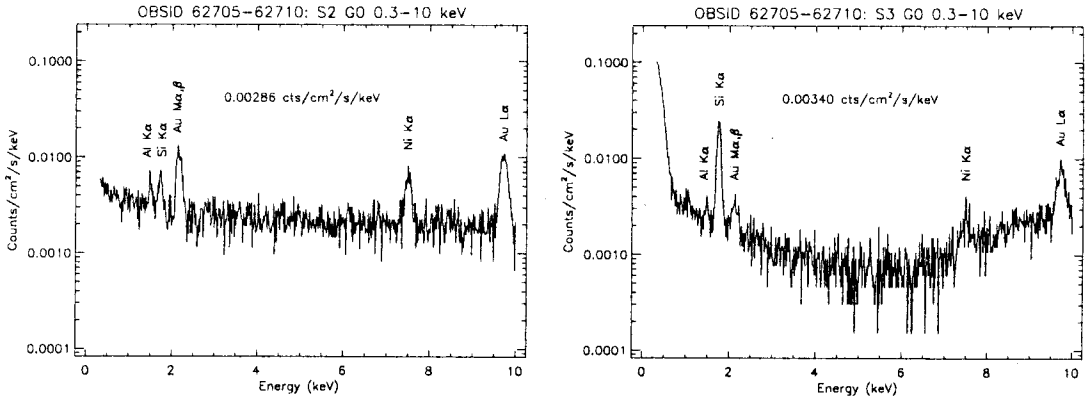

Figure 6.13: Energy spectra of the charged particle ACIS background (grade 0) with the HRMA doors closed. For a FI chip S2 (left) and a BI chip S3 (right). Line features are due to fluorescence of material in the telescope and focal plane.

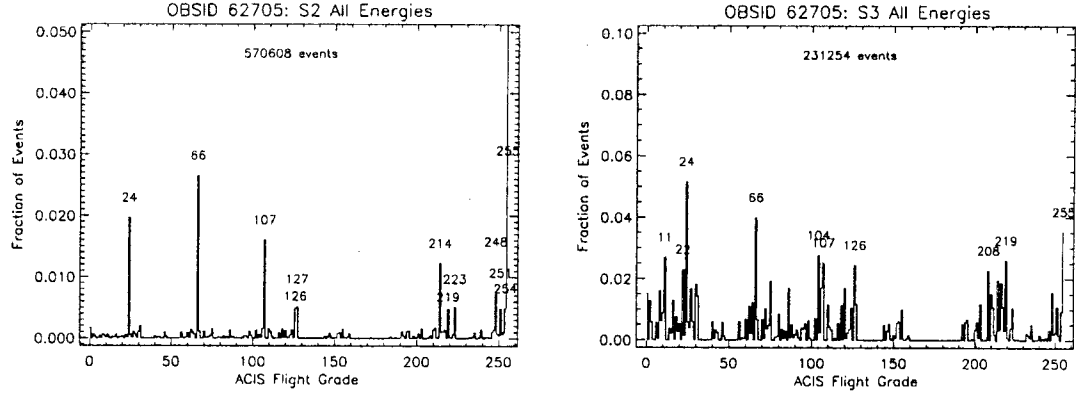

Figure 6.14: Fraction of ACIS background events as a function of grade from early in-flight data for an FI chip (S2) (left) and a BI chip (S3) (right).

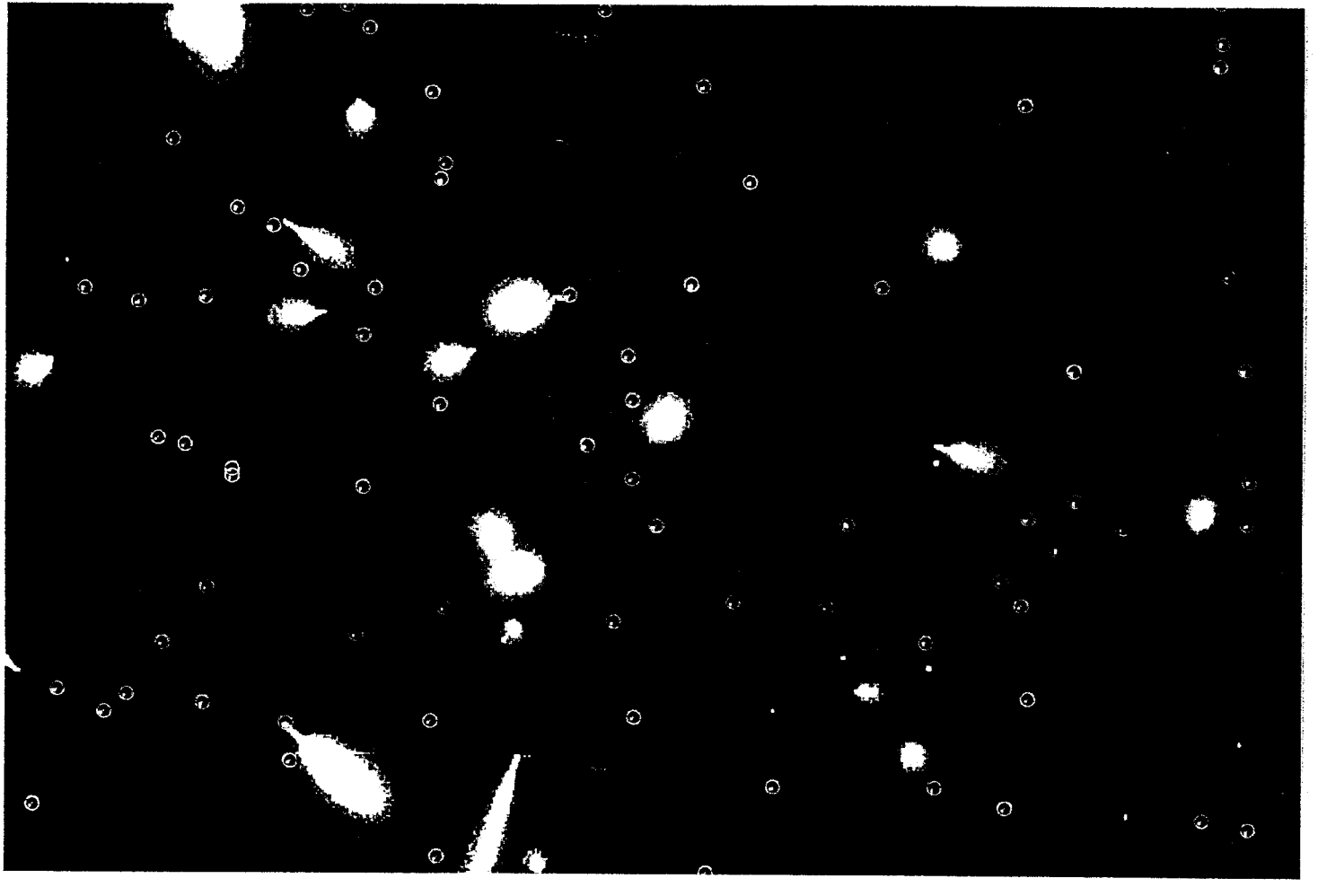

Data Processing Throughput

- Onboard data processors must reduce raw CCD datastream (e.g., $\sim$ 24 Mbits/s for ACIS) to meet spacecraft telemetry bandwith constraints (e.g., $\sim$ 24 kbits/s for *Chandra*).
- Event processing rates from an FI CCD for a typical timed-exposure observation (per 3.2s frametime):

Pixels examined :	1.05×10^6
Pixels above event threshold:	1.2×10^4
Events detected:	484
Event rejected by grade:	330
Events rejected by amplitude:	133
Events telemetered:	21

- Most of the 21 telemetered events are background events.
- Telemetry bandwidth available in this mode (to be shared by all operating CCDs) is 544 events per 3.2s frametime.

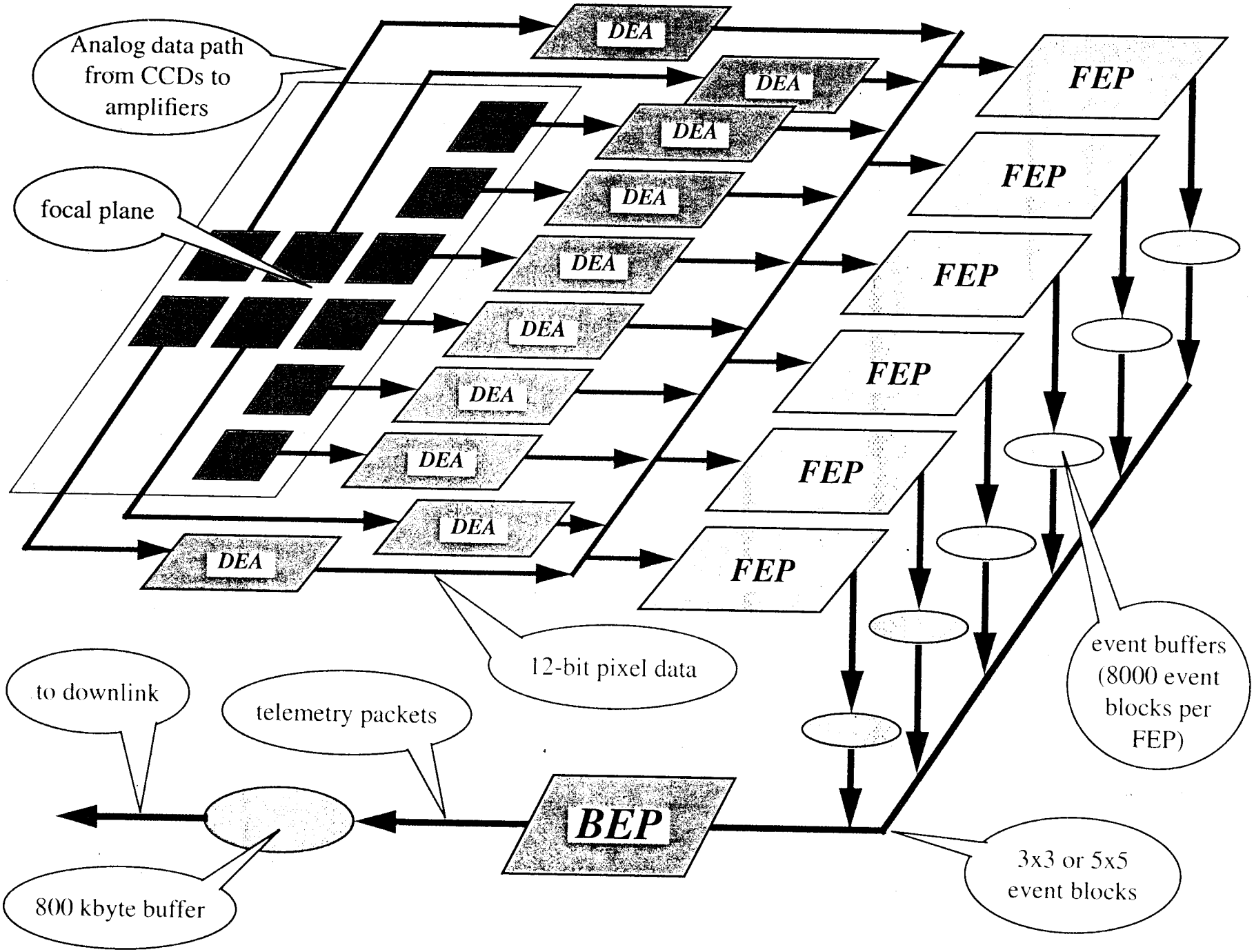
Analog data path from CCDs to amplifiers
focal plane
DEA
DEA
DEA
DEA
DEA
DEA
DEA
DEA
FEP
FEP
FEP
FEP
FEP
12-bit pixel data
event buffers (8000 event blocks per FEP)
to downlink
telemetry packets
BEP
800 kbyte buffer
3x3 or 5x5 event blocks

Table 6.6: Approximate on-orbit standard grade background counting rates with ACIS positioned at the ACIS-I aimpoint, T=-120C.

	Bkgrd rates (cts/sec)*						
Energy Band (keV)	I0	I1	I2	I3	S2	S3	I0123 avg
0.3-10	0.27	0.28	0.27	0.28	0.29	0.74	0.27
0.5-2	0.06	0.06	0.07	0.06	0.07	0.14	0.06
0.5-7	0.16	0.16	0.16	0.17	0.17	0.32	0.16
5.0-10	0.14	0.14	0.13	0.14	0.14	0.42	0.14
10-12	0.08	0.08	0.08	0.08	0.08	0.51	0.08

*Cts/s/chip, using only ASCA grades 02346, excluding background flares, bad pixels/columns and celestial sources identifiable by eye, Feb 2000 - Oct 2000 without gratings.

Table 6.7: Approximate on-orbit standard grade background counting rates with ACIS positioned at the ACIS-S aimpoint, T=-120C.

	Bkgrd rates (cts/sec)*						
Energy Band (keV)	I1	I2	I3	S1	S2	S3	S4
0.3-10	0.29	0.29	0.29	1.41	0.33	0.79	0.34
0.5-2	0.07	0.08	0.07	0.19	0.09	0.16	0.10
0.5-7	0.17	0.17	0.17	0.44	0.20	0.35	0.21
5.0-10	0.15	0.14	0.14	0.96	0.16	0.44	0.15
10-12	0.08	0.08	0.08	0.72	0.09	0.53	0.09

*Cts/s/chip, using only *ASCA* grades 02346, excluding background flares, bad pixels/columns and celestial sources identifiable by eye, Feb 2000 - Oct 2000 without gratings.

Table 6.10: Telemetry Saturation Limits

Mode	Format	Bits/event	Events/sec*	Number of Events in full buffer
CC	Graded	58	375.0	128,000
CC	Faint	128	170.2	58,099
TE	Graded	58	375.0	128,000
TE	Faint	128	170.2	58,099
TE	Very Faint	320	68.8	23,273

*(includes a 10% overhead for housekeeping data)

6.13.2 Telemetry Formats

There are a number of telemetry formats available. Specifying a format determines the type of information that is included in the telemetry stream. The number of bits per event depends on which mode and which format is selected. The number of bits per event, in turn, determines the event rate at which the telemetry will saturate and data will be lost until the onboard-buffer empties. The formats available depend on which mode (Timed Exposure or Continuous Clocking) is used. The modes, associated formats, and approximate event rates at which the telemetry saturates and one begins to limit the return of data, are listed in Table 6.10. The formats are described in the following paragraphs. Event "arrival time" is given relative to the beginning of the exposure in TE mode, or relative to read out in CC mode.

Faint Faint format provides the event position in detector coordinates, an arrival time, an event amplitude, and the contents of the 3 x 3 island that characterizes the event grade. The bias map is telemetered separately. Note that certain grades may be not be included in the data stream (section 6.10.1).

Graded Graded format provides event position in detector coordinates, an event amplitude, the arrival time, and the event grade. Note that certain grades may be not be included in the data stream (section 6.10.1).

Very Faint Very Faint format provides the event position in detector coordinates, the event amplitude, an arrival time, and the pixel values in a 5 x 5 island. As noted in Table 6.10, this format is only available with the Timed Exposure mode. Events are still graded by the contents of the central

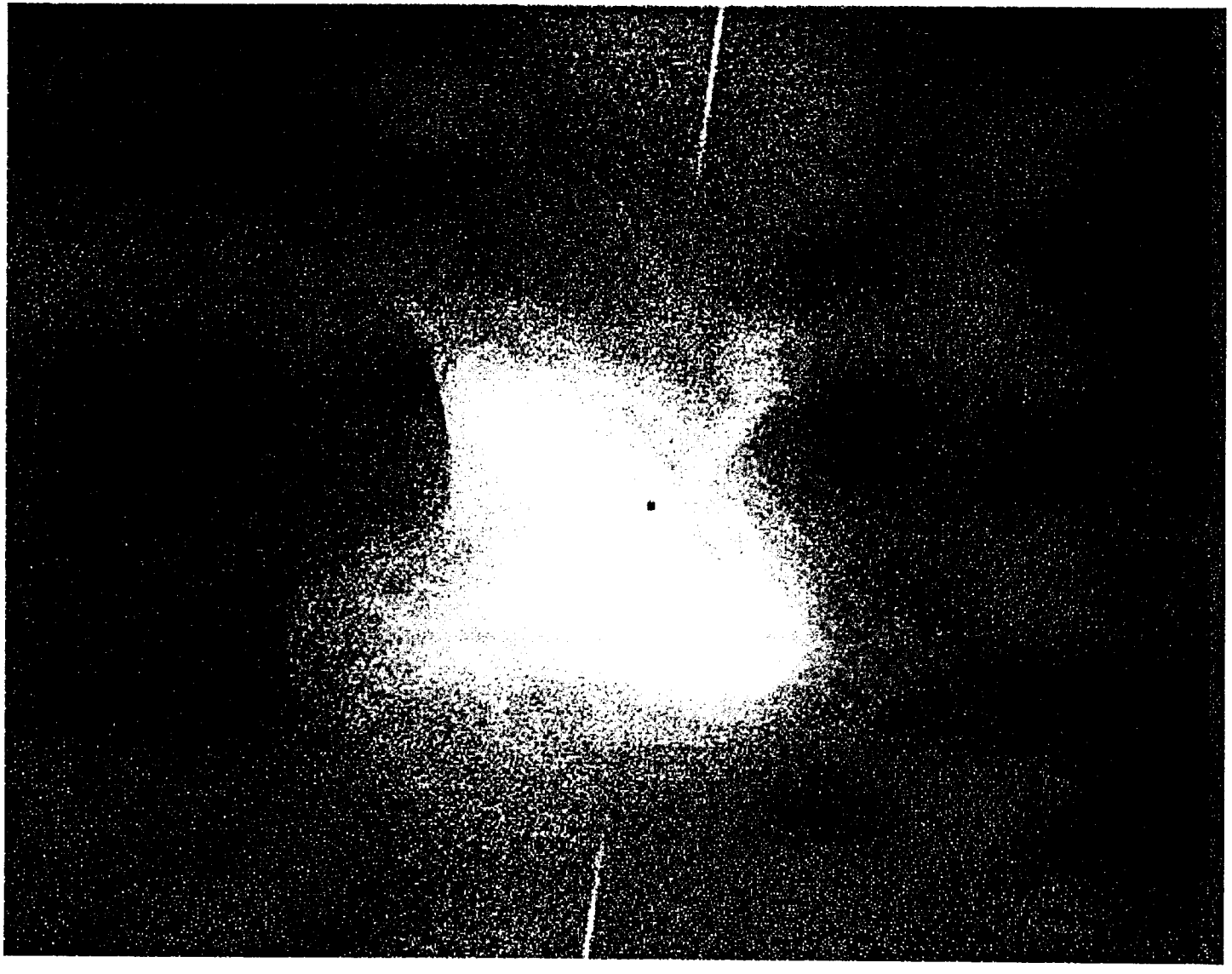

$E_1 = \bigstar$ $E_2 = \blacksquare\!\!\blacksquare$ $E_1 > E_2$

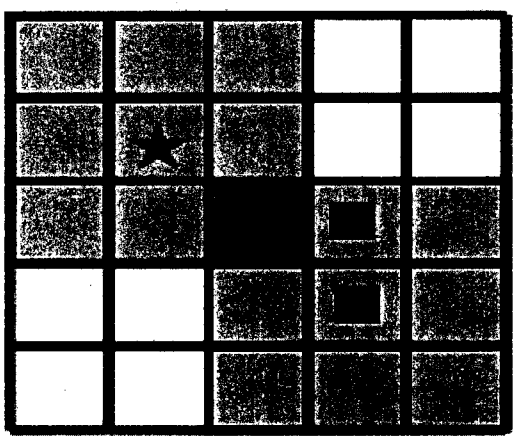

$E_1 ; E_2$

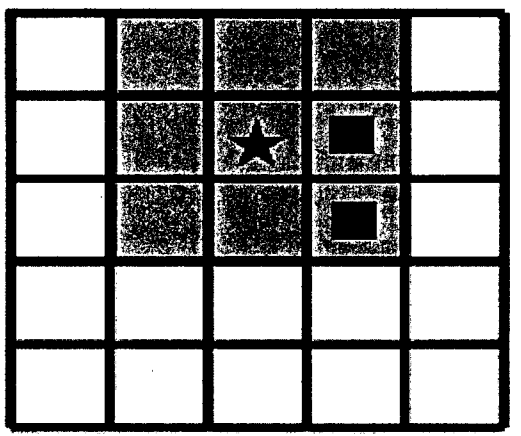

$E_1 + E_2$

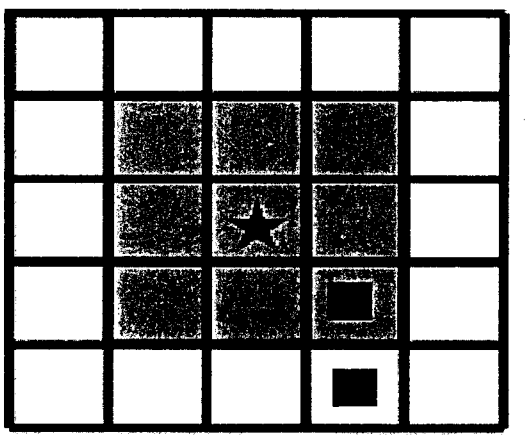

0

Pileup makes spectrum harder!

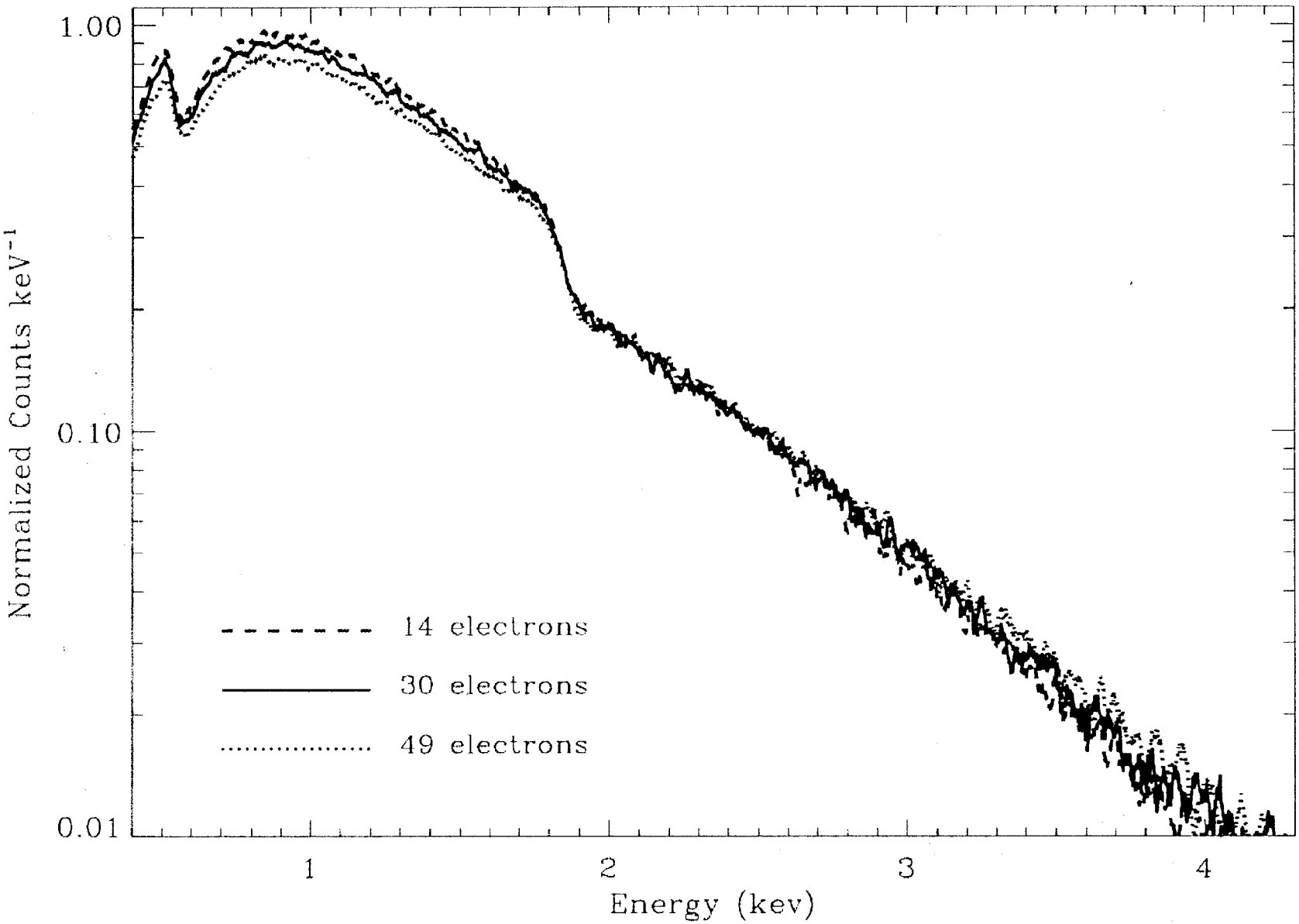

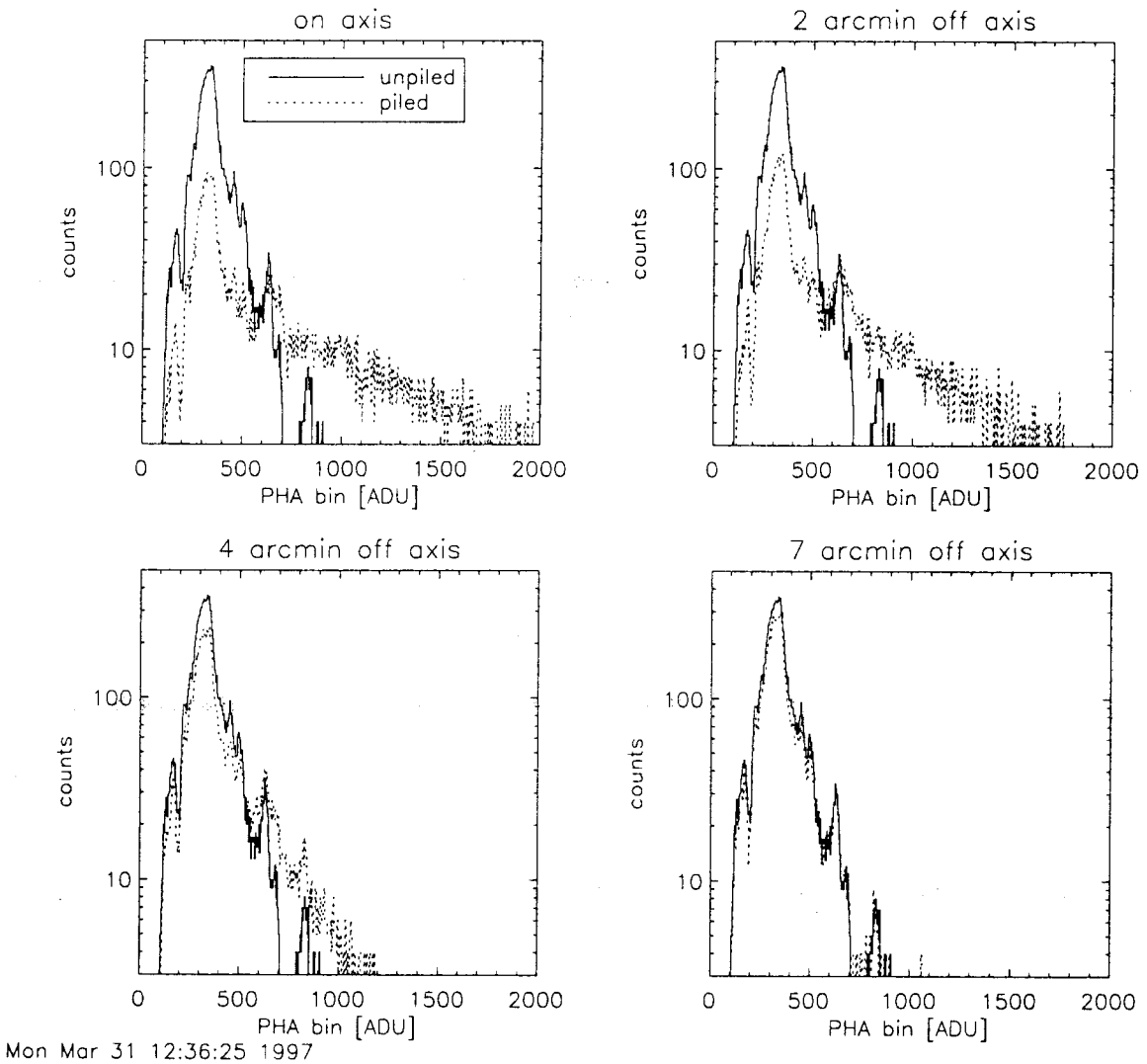

Figure 6.21: MARX simulations of the effect of pileup on the shape of the spectrum. The true (solid line) and the detected (dotted line) spectra are shown for four different viewing angles. The corresponding "pileup fractions" - see Section 6.16.2 - are 46%, 40%, 15%, and 2% as the image is moved progressively further off-axis. (Source: J. Kastner and M. Wise, *CXC*)

Table 6.9: CCD Frame Time (seconds) for Standard Subarrays

Subarray	ACIS-I (no. of chips)		ACIS-S (no. of chips)	
	1	6	1	6
1	3.0	3.2	3.0	3.2
1/2	1.5	1.8	1.5	1.8
1/4	0.8	1.1	0.8	1.1
1/8	0.5	0.8	0.4	0.7

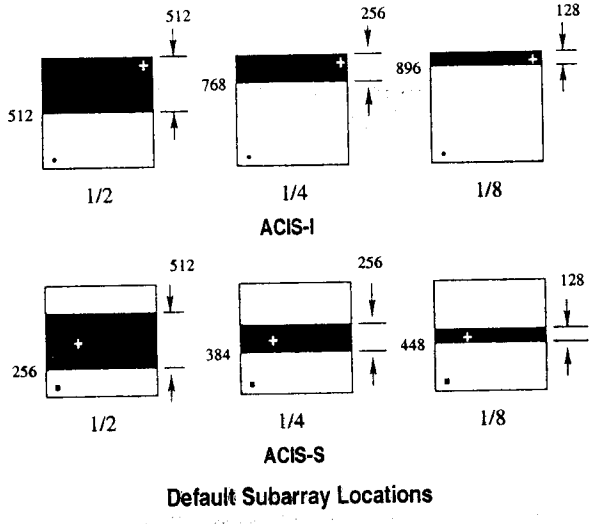

Figure 6.20: Examples of various subarrays. The heavy dot in the lower left indicates the origin

shown in Figure 6.20. The nominal frame time for a subarray depends on (q), (n), and the total number of CCDs that are activated (m) – see Table 6.9. The nominal frame time is given by:

$$T(msec) = 41 \times \mathrm{m} + 2.84 \times \mathrm{n} + 5.2 + 0.040 \times (\mathrm{m} \times \mathrm{q}).$$

As with full frames (section 6.12.2), selecting a frame time less than the optimum results in loss of observing efficiency.

6.12.4 Trailed Images

It takes 40 μsec to transfer the charge from one row to another during the process of moving the charge from the active region to the framestore region.

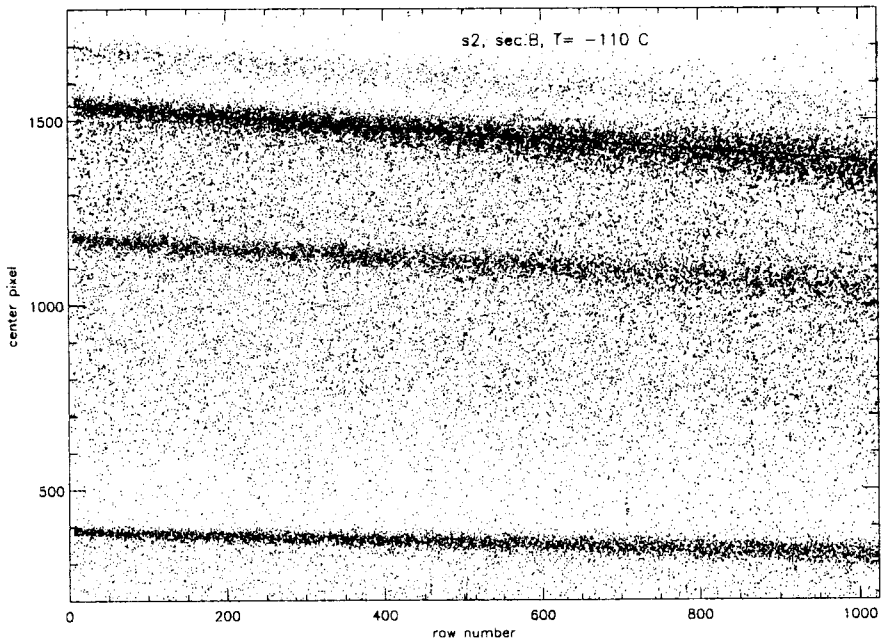

Figure 1. Pulseheight of the center pixel as a function of row number at -110 C for the damaged flight device S2.

of magnitude higher dark current at the same temperature. Also, the dependence of the CTI on temperature looked different for the ground irradiated chips.

We started to look for another type of damaging irradiaion which could produce flight-like results. There seem to be no data in the literature on the damage caused by low energy protons (100 – 200 keV) and we implemented a series of experiments irradiating CCDs with low energy protons. The most credible explanation now seems to be that the damage was caused by the low energy protons leaking through the telescope mirror during the radiation belt passages. The detailed discussion of the Chandra radiation environment and the details of the mechanism of the proton penetration through the telescope structure will be discussed in another talk presented at this conference.[1] In this paper in the sections 2,3 we focus on the mechanism of the damage in the CCDs and the techniques we have developed to measure electron trap parameters. In section 4 we describe a squeegee technique which was developed as a method to improve CTI by supplying some fat zero charge to fill the traps. This techique turned out to be a very efficient way to measure trap parameters.

2. CHARACTERIZATION OF THE DAMAGE IN THE FLIGHT DEVICES

One of the most meaningful ways to demonstrate the transfer inefficiency in a CCD is to plot the pulseheight of an X-ray event as a function of row number when the CCD is illuminated with the monochromatic source of X-rays. A typical example of such a plot for the damaged flight device S2 looking at the calibration source is shown in Fig. 1. The focal plane temperature during this measurement was maintained at -110^0 C. Each dot in this plot represents an amplitude of the center pixel of an X-ray event, pixels adjacent to the center being ignored. Three emission lines can be clearly seen in the source spectrum as areas with the high density of the dots: $Al\ K$, $Ti\ K$ and $Mn\ K_\alpha$. Much weaker $Mn\ K_\beta$ can also be observed near the top of the plot. The amplitude of the pulseheight for each of the emission lines gets smaller at the higher row numbers as charge packets lose charge in every transfer from pixel to pixel. In the beginning of the mission each emission line on this plot was absolutely flat, the width of each line also stayed the same across the entire device.

Extremely important feature of this plot is that the pulseheight-vs-row dependence is linear near the bottom of the image section and does not have a roll off or flattening at small row numbers. This is a strong indicator that unlike the image section of the device the frame store section was not damaged. When the frame store is irradiated and electron traps are introduced into its transfer channel, charge packets formed near the bottom of the image section will travel through the empty traps in the frame store section and experience much heavier charge losses than

Physics of Radiation-induced Charge Transfer Inefficiency

- Photoelectrons (and secondary ionization) liberated by an incident X-ray are not really "free"; they occupy conduction band states.
- The existence of the conduction band depends on the symmetric arrangment of atoms in the lattice.
- When the lattice is damaged by incident particles (such as protons), its symmetry is disrupted.
- Electron "traps" (new, localized bound states) can be associated with radiation-induced lattice disruptions.
- If electrons encounter such traps during the readout process, they can be left behind, and thus lost from the X-ray induced charge packet. Eventually, trapped electrons can be released via thermal excitation.
- Since the loss process is stochastic, (especially in the presence of random background charged particle radiation) the traps degrade the spectral resolution.

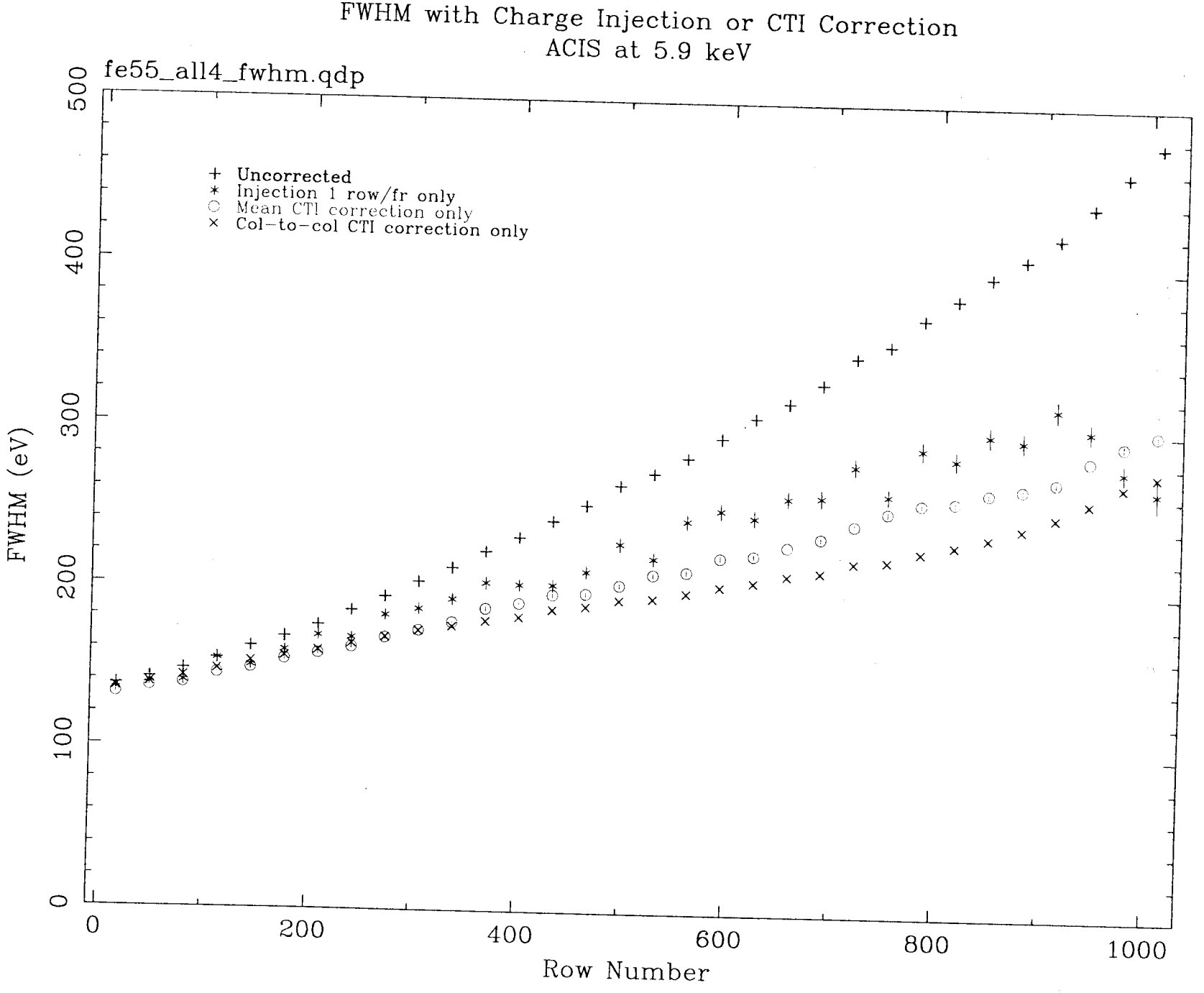
FWHM with Charge Injection or CTI Correction
ACIS at 5.9 keV
fe55_all4_fwhm.qdp
+ Uncorrected
* Injection 1 row/fr only
○ Mean CTI correction only
× Col-to-col CTI correction only
FWHM (eV)
Row Number
0
100
200
300
400
500
0
200
400
600
800
1000

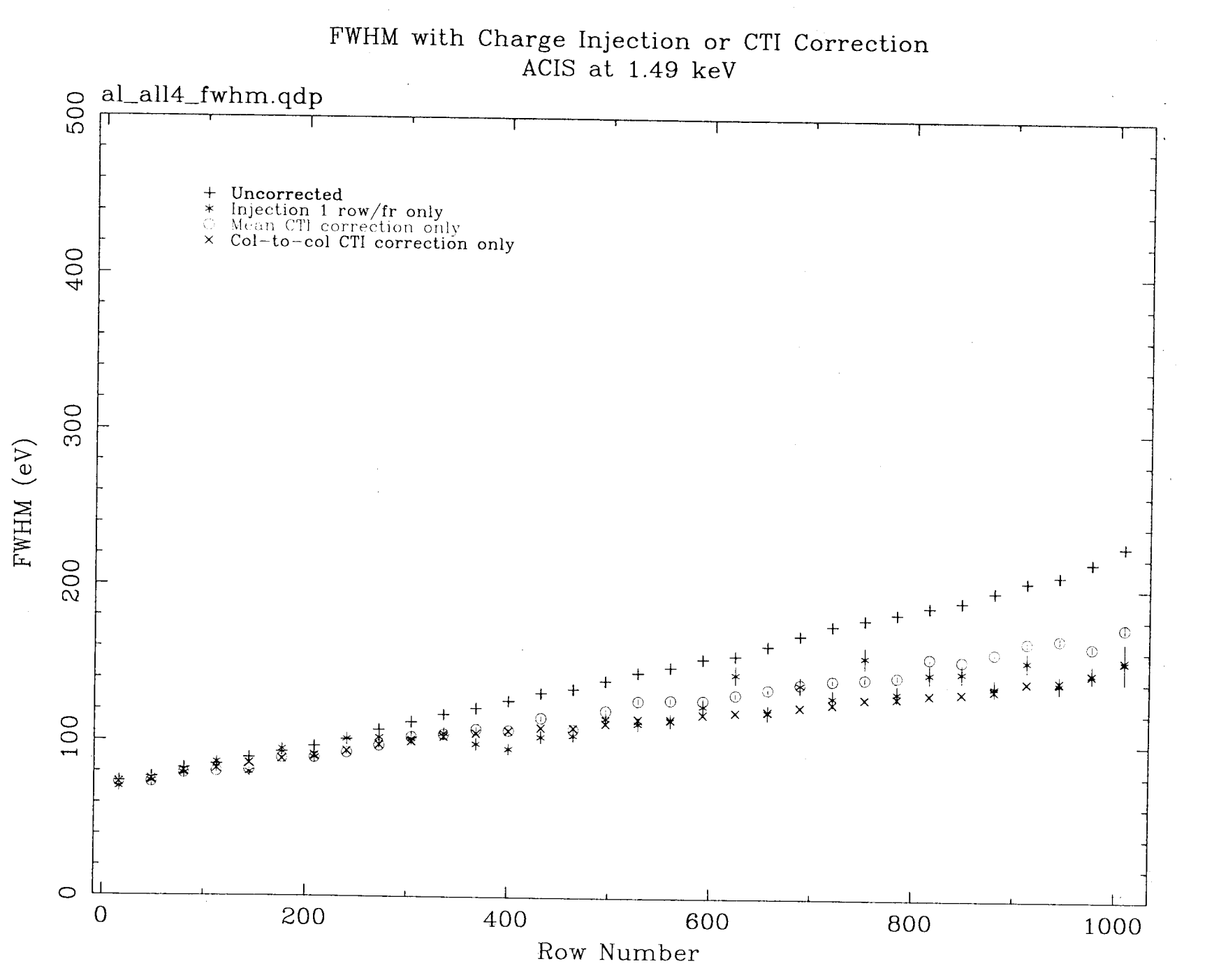
FWHM with Charge Injection or CTI Correction
ACIS at 1.49 keV
al_all4_fwhm.qdp
+ Uncorrected
* Injection 1 row/fr only
○ Mean CTI correction only
× Col-to-col CTI correction only
FWHM (eV)
0
100
200
300
400
500
0
200
400
600
800
1000
Row Number

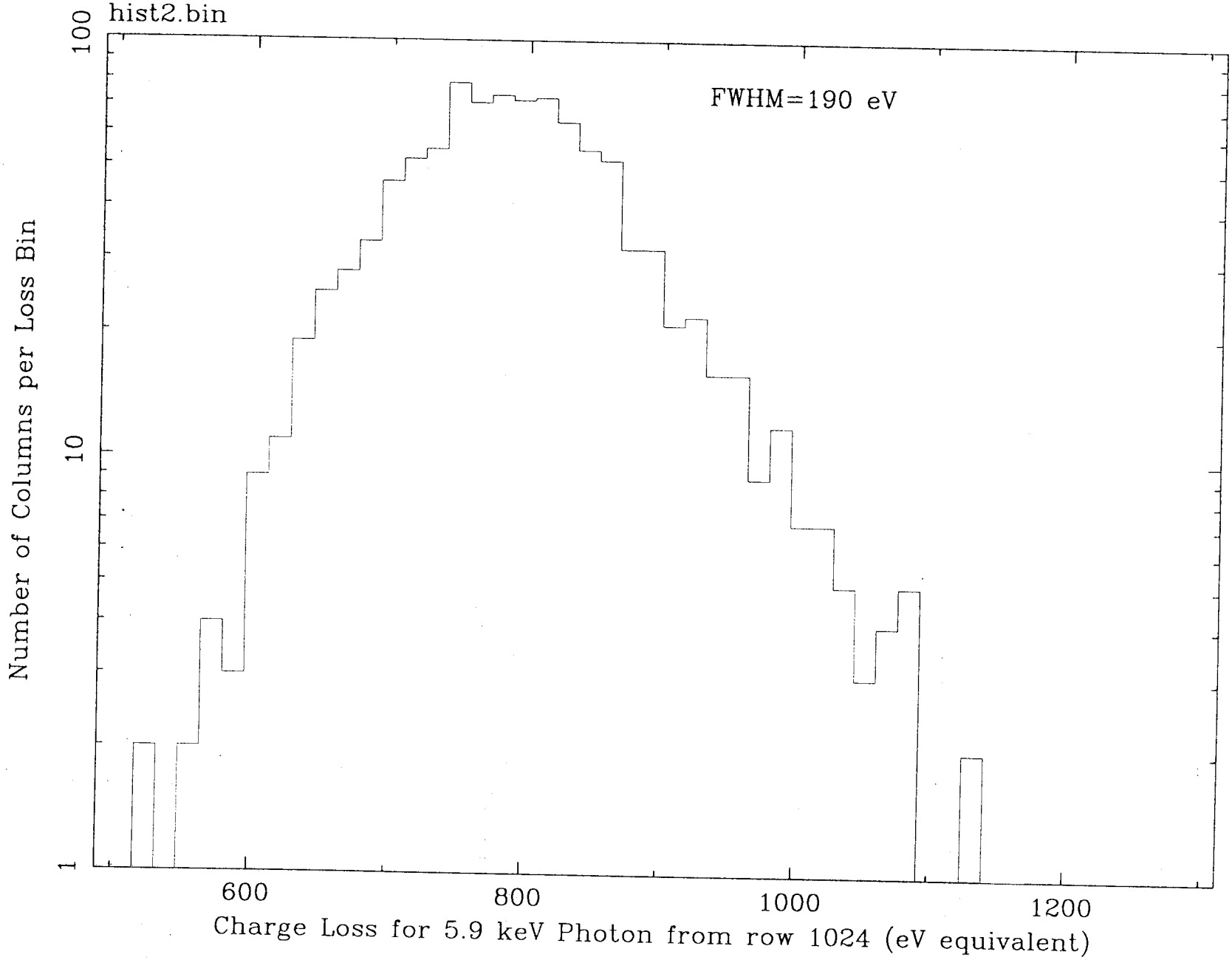
Column-to-column non-uniformity in ACIS FI Detector I3
5.9 keV
hist2.bin
FWHM=190 eV
Number of Columns per Loss Bin
100
10
1
600
800
1000
1200
Charge Loss for 5.9 keV Photon from row 1024 (eV equivalent)

CCDs X-ray Detectors in the Future

- Photon-counting X-ray CCDs are currently operating on two major, long-duration (5 - 10 year) observatory missions (*Chandra* and *XMM-Newton*) and on one small mission (*HETE-2*). New X-ray CCD instruments are planned for launch on at least two medium-sized missions (*SWIFT* and *Astro-E2*) within the next three years.
- Micro-calorimeter detectors (e.g., Astro-E2's XRS) will provide a factor of 10-20 improvement in spectral resolution, but are unlikely to provide megapixel imaging, or good detection efficiency at very low energies (E$<$ 0.5 keV), within the next 5 years. For this reason Constellation-X (launch $\sim$ 2010?) will include CCD detectors for grating readout.
- Desirable improvements in megapixel imagers:
  - $\star$ Better low-energy response (efficiency and spectral resolution) to study the high-redshift universe
  - $\star$ Better radiation tolerance to support long mission life
  - $\star$ Better time resolution/ faster readout rates (lower optical blocking losses, higher operating temperatures, improve pileup threshold.)
- Various technologies are being explored to provide these improvements.

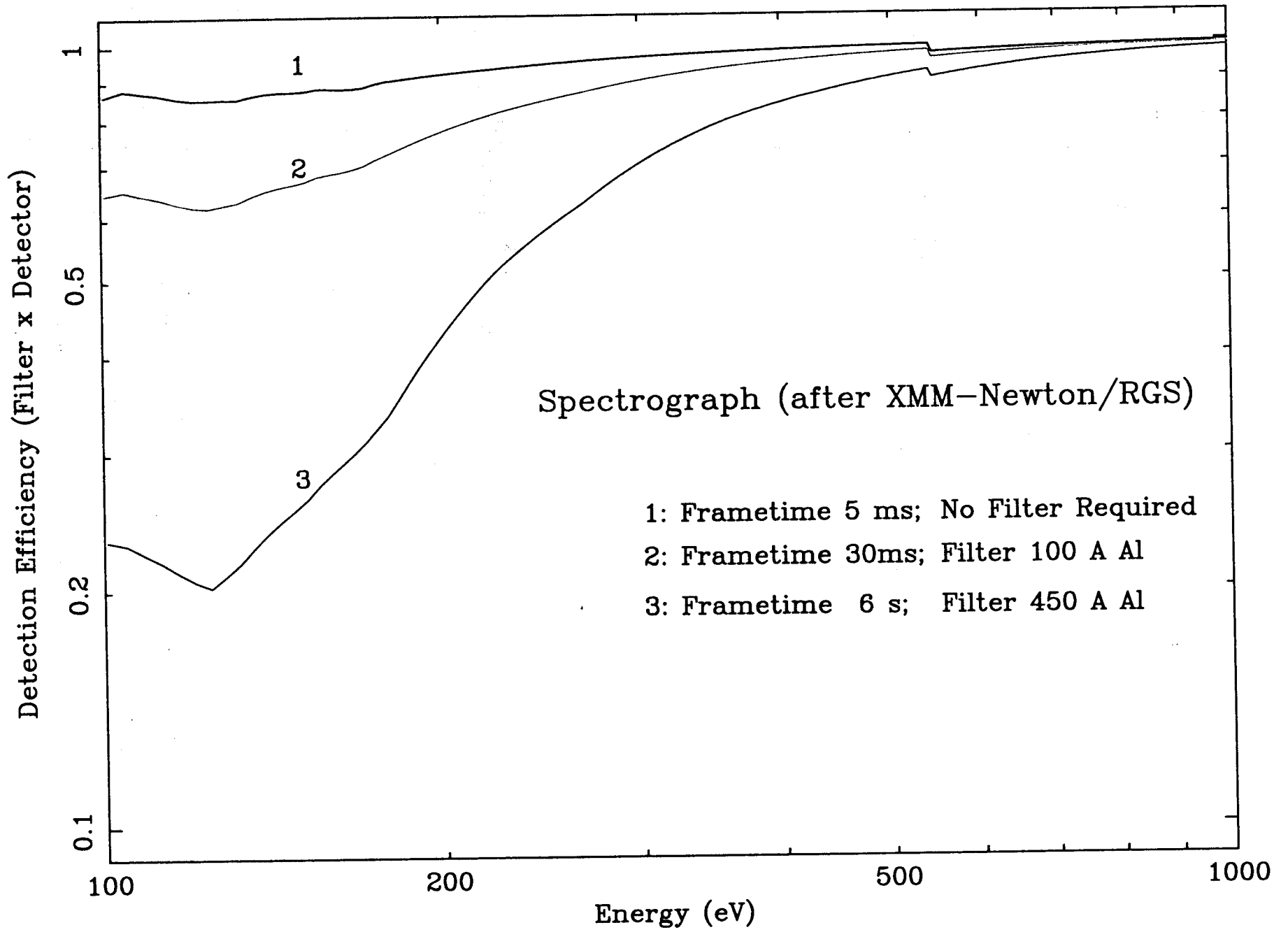
Detection Efficiency (Filter x Detector)
1
0.5
0.2
0.1
100
200
500
1000
Energy (eV)
1
2
3
Spectrograph (after XMM−Newton/RGS)
1: Frametime 5 ms; No Filter Required
2: Frametime 30ms; Filter 100 A Al
3: Frametime 6 s; Filter 450 A Al

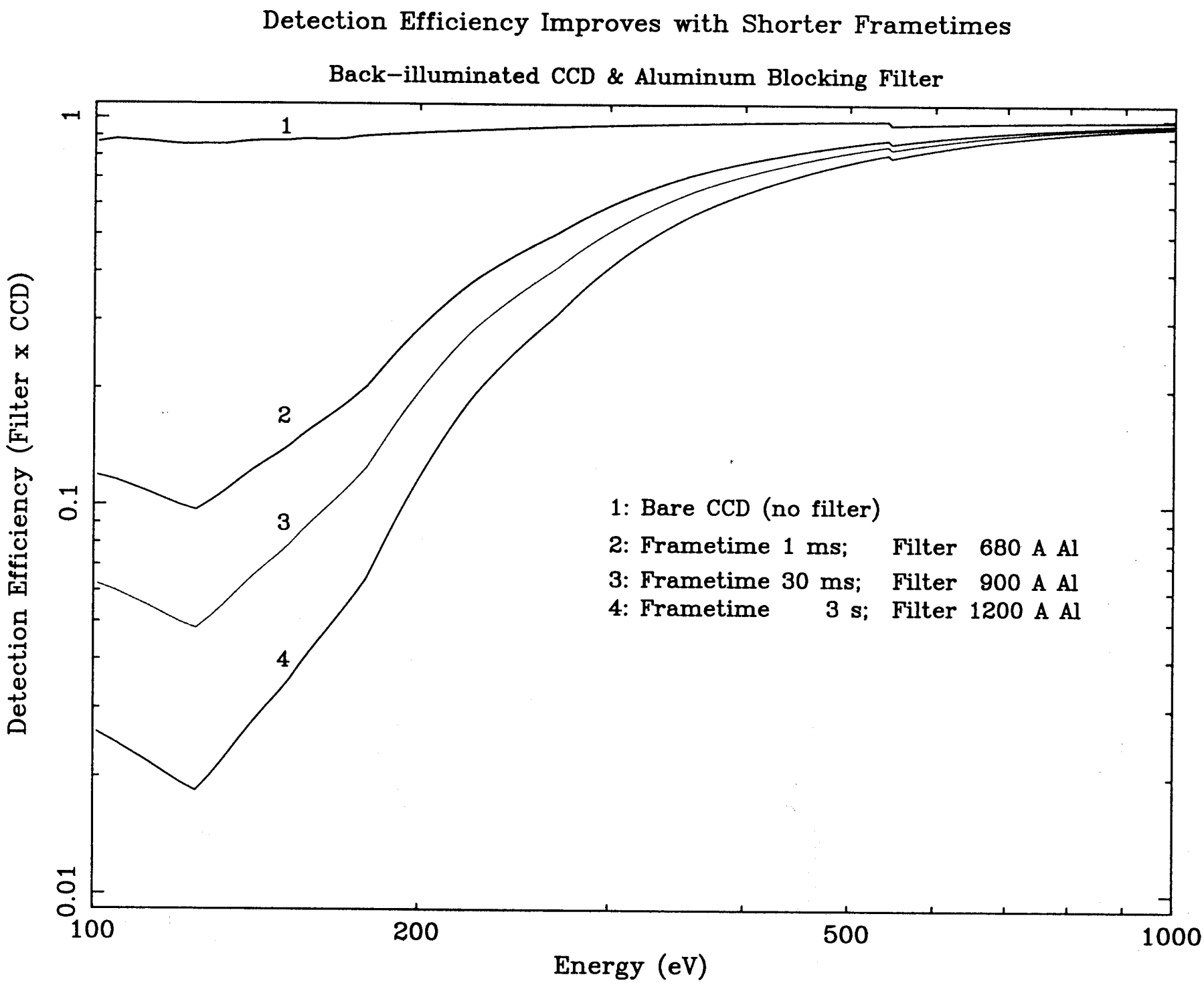
Detection Efficiency Improves with Shorter Frametimes
Back-illuminated CCD & Aluminum Blocking Filter
Detection Efficiency (Filter x CCD)
1
0.1
0.01
100
200
500
1000
Energy (eV)
1
2
3
4
1: Bare CCD (no filter)
2: Frametime 1 ms; Filter 680 A Al
3: Frametime 30 ms; Filter 900 A Al
4: Frametime 3 s; Filter 1200 A Al